



Erasmus Mundus Joint Master degree
Photonics for Security Reliability and Safety

Master *Photonics for Security Reliability and Safety* (PSRS)



CHARACTERIZATION OF SCANDIUM-DOPED ALUMINUM NITRIDE THIN FILMS FOR BULK ACOUSTIC WAVE RESONATORS

Master Thesis Report

Presented by
Kapil Saha

and defended at the
University Jean Monnet

30th August 2023

Academic Supervisor:
Dr. Carlo Ricciardi

Host Supervisor:
Dr. Matteo RINALDI
Dr. Luca COLOMBO
Dr. Pietro SIMEONI

Jury Committee:
Dr. Carlo Ricciardi
Dr. Jyrki Saarinen

**CHARACTERIZATION OF SCANDIUM-DOPED ALUMINUM
NITRIDE THIN FILMS FOR BULK ACOUSTIC WAVE
RESONATORS**

Master Thesis Report

Kapil Saha
August 2023

Master Photonics for Security Reliability and Safety (PSRS)

Abstract

The current research focuses on examining the effect of Scandium (*Sc*) doping on Aluminum Nitride (*AlN*) thin films with respect to the performance of MEMS piezoelectric resonators. The primary objective of this work is to analyze the impact of Scandium doping on the structural, morphological, and piezoelectric characteristics of thin films. Additionally, the research project aims to assess the effectiveness of these films in applications involving BAW resonators. The present study is structured into three five chapters. The initial chapter serves as an introductory section for the thesis, providing an overview of the current advancements in the field of MEMS resonators. Additionally, it discusses into the fundamental principles of piezoelectricity and ferroelectricity, which are the primary technologies investigated in this research endeavor. The subsequent part of the study centers on the methodologies employed for producing Scandium Aluminum Nitride (*ScAlN*) thin films, wherein the Scandium doping concentrations are varied. The achievement of precision control over doping levels and film qualities is facilitated through the systematic manipulation of deposition parameters, including temperature, pressure, chuck height, gas flow, and dopant precursor concentrations. The third chapter of the dissertation elucidates the technique used proceed for characterizing the manufactured *ScAlN* thin films. The stress exerted following the deposition of *ScAlN* is measured using a laser scanning approach. The X-ray diffraction (XRD) approach is employed to ascertain the crystal structure and phase orientation, whereas scanning electron microscopy (SEM) and atomic force microscopy (AFM) are utilized to examine the topology, morphology, and surface roughness of the films. The succeeding section present the effects of varying doping levels of *Sc* on the surface topography, crystal structure, and applied stress of *AlN* thin films. In the final section, an evaluation on the piezoelectric response of the films is conducted by means of measuring the piezoelectric coefficient (d_{33}) by using of the Double Beam Laser Interferometry (DBLI) technique. The initial section of the discourse focuses on the examination of the ferroelectric characteristic exhibited by *ScAlN*. This section provides a concise introduction to the aixACCT DBLI instrument, followed by a detailed explanation of the building procedure employed for the sample capacitors utilized in the extraction of the piezoelectric coefficient d_{33} . Based on the observations detailed in this chapter, the incorporation of Scandium as a dopant has been found to exert a substantial influence on the characteristics of Aluminum Nitride (*AlN*) thin films in comparison to their undoped equivalent. The thin films of *ScAlN* demonstrate enhanced piezoelectric response, suggesting the possibility of enhanced performance in BAW resonators. The d_{33} value of 13.5 pm/V was obtained from measurements conducted on a sample of *ScAlN* thin films with a doping level of 30%. This study presents a comparative investigation of the piezoelectric effect shown by samples consisting of various *Sc*-doped *AlN* thin films. The last chapter provides a short overview of the principal findings of the study, offering valuable insights that may contribute to the enhancement and development of forthcoming BAW resonators. The present study has expanded the potential for further investigation in defining the ferroelectric behavior of *ScAlN* and exploring the effects of doping *ScAlN* with additional materials to enhance its performance.

Acknowledgement

I would like to express my gratitude to Professor Matteo Rinaldi for providing me with the opportunity to engage in research within his research group. I would like to express my gratitude to Dr. Luca Colombo, the Assistant Research Professor, and the Principal Investigator of my thesis project Dr. Pietro Simeoni who provided guidance and support during my thesis. Pietro's assistance has been crucial in my professional and personal development as a researcher.

I would also like to express my gratitude to all the individuals affiliated with the SMART center at Northeastern University for their invaluable assistance and encouragement. I would like to extend my heartfelt appreciation to Dr. Stefan Johann Rupitsch, Dr. Dragan Damjanovic, Dr. Simon Fichtner, and Dr. Niklas Wolff for their scholarly publications, which have greatly contributed to my understanding and knowledge of this subject matter. Additionally, I included certain elements of their works into my dissertation. I express my gratitude to the publishing companies for granting me the necessary copyright permissions to utilize those works for a limited timeframe.

I would like to express my gratitude to my acquaintances, professional associates and friends who supported me the whole time when I faced challenges. I would like to convey appreciation to my academic supervisor Dr. Carlo Ricciardi and program coordinator Dr. Nathalie Destouches to give me the chance to participate in this program and to enrich my skillset essential for my future endeavor.

I would like to express my sincere gratitude to my family, including my parents, and brother for the exceptional level of support they have provided me throughout the preceding years that gave me the opportunity to explore my potential here. Their unwavering support has played a pivotal role in shaping the current circumstances I find myself in. I take tremendous pride in this achievement, and I attribute a significant portion of it to their contributions, for which I am profoundly appreciative. I would want to express my gratitude to my girlfriend, Progga, whose virtual presence has been important in helping me navigate the challenging months that have transpired.

I would like to express my sincere gratitude to all those who have consistently provided me with support, whether through direct or indirect means. While the thesis represents my individual effort, I firmly believe that this achievement is a collective endeavor, in which each and every one of you has played a significant role.

Table of Contents

Abstract	i
Acknowledgement	ii
Table of Contents	iii
Table of Figures	iv
Chapter 1: Introduction	1
1.1 Introduction.....	1
1.2 Micro-Electromechanical Systems (MEMS)	1
1.3 Bulk Acoustic Wave Resonators (BAWRs)	2
1.4 Piezoelectricity	3
1.4.1 Physics of piezoelectricity	3
1.4.2 Electromechanical coupling factor	6
1.4.3 Piezoelectric materials	7
1.5 Ferroelectricity	7
1.5.1 Introduction to ferroelectricity	7
1.5.2 Ferroelectric hysteresis loop	9
Chapter 2 : Deposition techniques	13
2.1 Magnetron sputtering.....	13
2.3 Deposition of $Sc_xAl_{1-x}N$ film.....	16
2.4 Detecting the doping level of Scandium	18
2.5 Realizing deposition rate of $Sc_xAl_{1-x}N$ thin films.....	19
Chapter 3 : Characterization of $Sc_xAl_{1-x}N$ thin films	22
3.1 Stress measurement	22
3.2 Crystallinity of the deposited films	24
3.2.1 Detecting crystallographic orientation using XRD technique	25
3.2.2 Detecting Rocking Curve (RC) using XRD technique.	28
3.2.3 Detecting crystal phases using XRD technique	31
3.3 Detection of AOG's using SEM.....	33
3.4 Surface topography with AFM	38
3.4.1 Surface imaging	38
3.4.2 Surface roughness detection	42
Chapter 4 : Piezoelectricity of the $ScAlN$ thin films	44
4.1 Ferroelectric behavior of $ScAlN$	44
4.2 Piezoelectric coefficients of $ScAlN$	45
4.2.1 Sample preparation	46
4.2.2 aixACCT DBLI.....	49
4.2.3 d_{33} measurement	50
4.3 Polarization-Displacement curve	53
Chapter 5 : Conclusions and future research scopes	54
Bibliography	56
Statement of non-plagiarism	59
Supervisor approval	60
Copyrights	61

Table of Figures

Figure 1.1: A quartz crystal structure with metal electrodes on top and bottom. In a) the crystal is in its initial state, with no mechanical load applied. The longitudinal and transverse piezoelectric effects are depicted in b) and c), respectively. The charge centers, CQ+ and CQ-, are also included [11].	4
Figure 1.2: A polycrystalline ferroelectric with grains that are randomly oriented before and after poling [14]	9
Figure 1.3: Strain–electric field (x –E) hysteresis loop (butterfly loop) in ferroelectrics: (a) idealized loop in a crystal where polarization changes by only 180°, and (b) real polarization and strain loops measured on (111)-oriented, 322 nm thick, sol-gel $PbZr_{0.53}Ti_{0.47}O_3$ thin film [14].	10
Figure 2.1: Schematic illustration of magnetron sputtering system [20]	14
Figure 2.2 Sc doping percentage and $ScAlN$ deposition rate correlation with Scandium to Aluminum power ratio	20
Figure 3.1 Variation of stress with the Sc to Al generator power ratio	23
Figure 3.2: Dependence of film stress level on N_2 flow rate	24
Figure 3.3 Gonio scan (2θ scan) data plotted for the films with Sc doping level of 10% - 45% deposited on Si (100)	26
Figure 3.4: 2θ scan data plotted for the films with Sc doping level of 10% – 40% deposited on Pt	28
Figure 3.5 Omega Scan (ω scan) data of $Sc_xAl_{1-x}N$ ($x = 0.10, 0.20, 0.30, 0.35, 0.40, 0.45$) deposited on Si substrate with RC value	29
Figure 3.6 Omega Scan (ω scan) data of $Sc_xAl_{1-x}N$ ($x = 0.10, 0.20, 0.30, 0.40, 0.45$) deposited on Pt layer with RC value	31
Figure 3.8 Angle vs Intensity plot from $\theta - 2\theta$ scan data deposited on Pt layer with filtered data.	32
Figure 3.7 Angle vs Intensity plot from $\theta - 2\theta$ scan data deposited on Pt layer.	32
Figure 3.9 Schematic of SEM procedure	34
Figure 3.10 SEM images of $ScAlN$ thin films deposited on Si	35
Figure 3.11 SEM images of $ScAlN$ thin films deposited on Pt layer.	37
Figure 3.12 Interatomic interaction forces acting in AFM process.	38
Figure 3.13 Schematic diagram of AFM scanning procedure	39
Figure 3.14 AFM scan images of the $ScAlN$ films deposited on Si	40
Figure 3.15 AFM scan images of the $ScAlN$ films deposited on Pt	41
Figure 3.16 Variation of surface roughness with Sc to Al generator power ratio	43
Figure 4.1 The polarization-electric field (P-E) hysteresis loops of ferroelectric $Al_{1-x}Sc_xN$ with Sc concentrations ranging from $x = 0.27$ to $x = 0.43$, as well as the P-E loop	

of PZT 52/48, were examined. The structures associated with the distinct polarization states are depicted on the right [12]..... 45

Figure 4.2 The lithographic mask created in K-Layout environment represents the top electrode shapes..... 47

Figure 4.3 The final chip look showing the top electrode pattern with Gold (Au). 48

Figure 4.4 Schematic of the optical setup for the aixACCT DBLI measurement tool... 49

Figure 4.5 A demonstration of the laser placement and examination of a 3 mm circle ferroelectric capacitor. 51

Figure 4.6 Change in d_{33} values with Sc to Al generator power ratio. 52

Figure 4.7 polarization – displacement curve in time domain for our *ScAlN* samples with different Sc% 53

Chapter 1: Introduction

1.1 Introduction

This thesis report focuses on the characterization of scandium-doped aluminum nitride ($ScAlN$) thin films for bulk acoustic wave resonators. The introduction of scandium into the AlN lattice offers a promising approach to improving the piezoelectric properties and overall performance of the thin films. Scandium doping has the potential to enhance the electromechanical coupling coefficient, temperature stability, and power handling capacity of BAWRs.

The main objective of this research is to investigate and understand the impact of scandium doping on the structural, electrical, and piezoelectric properties of AlN thin films. Through a comprehensive characterization process, including thin film deposition, structural analysis, electrical measurements, and piezoelectric characterization, the thesis aims to unfold the influence of scandium incorporation to the performance of BAWRs.

The thesis report is organized as follows: Chapter 1 provides an extensive literature review on Microelectromechanical Systems (MEMS), bulk acoustic wave resonators (BAWR), aluminum nitride thin films, Physics behind Piezoelectricity and Ferroelectricity of the materials, and the role of scandium doping in enhancing their properties. Chapter 2 details the experimental methodology, including thin film deposition techniques, characterization methods, and measurement setups employed in the research. Chapter 3 presents the results obtained from structural analysis, electrical measurements, and state of art of piezoelectric efficiency characterization of the $Sc_xAl_{1-x}N$ thin films. Chapter 4 thoroughly discusses the findings, analyzes the influence of scandium doping on the properties of the thin films, and provides insights into the optimization of $Sc_xAl_{1-x}N$ thin films for advanced BAWRs. Finally, Chapter 5 summarizes the conclusions derived from the research and outlines potential future directions in the field.

By characterizing scandium-doped aluminum nitride thin films for bulk acoustic wave resonators, this thesis contributes to the advancement of piezoelectric materials for high-performance BAWRs. The outcomes of this research are expected to facilitate the development of improved BAWR designs with enhanced frequency selectivity, improved linearity, and higher power handling capabilities. Such advancements will support the evolution of wireless communication systems and enable the realization of efficient, compact, and high-performance devices for various applications ranging from wireless connectivity to radar systems and beyond.

1.2 Micro-Electromechanical Systems (MEMS)

MEMS have proven to be game changers in a range of disciplines, including telecommunications, transportation, health care, the internet of things (IoT), and general automation. MEMS technology produces tiny integrated mechanical and electrical devices that range in size from a few micrometers to millimeters and are

manufactured utilizing integrated circuit (IC) batch processing [1]. These devices can detect, control, and activate microscopically, resulting in macroscale impacts. MEMS are defined as any device with moving parts or fluid in the μm - mm range that is manufactured using a photolithography process [2]. Typically, they are fabricated using semiconductor manufacturing techniques including photolithography, deposition, etching, and packaging. The system is the integration of mechanical elements, sensors, resonators, actuators, and electronics on a single microscale or nanoscale silicon substrate.

Our current study on microelectromechanical systems is mostly focused on BAW resonators. Among all resonant devices, acoustic wave resonator is a specific type of MEMS resonator. These devices harness the propagation of acoustic waves and exhibit natural vibrations at a resonance frequency that is determined by their dimensional characteristics and mechanical material properties [3]. To introduce the concept of BAW resonators, we need to know about MEMS resonator. The MEMS resonator is a micromachined mechanical structure that vibrates at its natural resonance frequency in response to external excitations [4]. They have become integral components in a wide range of electronic devices, offering precise frequency control and filtering capabilities. These resonators utilize the process of miniaturization and integration of mechanical and electrical components onto a singular chip in order to provide solutions that are compact, consume low power, and exhibit high performance. The integration of various components within a device obviates the necessity for large external components and interconnections, thereby yielding devices that are both compact and highly integrated.

1.3 Bulk Acoustic Wave Resonators (BAWRs)

Bulk Acoustic Wave Resonators (BAWRs) are fundamental components in modern wireless communication systems, providing high-quality frequency selection and filtering capabilities [5]. They offer exceptional frequency stability, a superior quality factor (Q factor), and compatibility with integrated circuit technologies. BAW resonators are dependent on the transmission of acoustic waves, specifically longitudinal or transverse waves, within the piezoelectric substance. The propagation of these waves within the material occurs as mechanical vibrations, thereby eliciting an electrical reaction because of the inherent piezoelectric characteristics [6]. A piezoelectric substance, such as quartz, aluminum nitride (AlN), or scandium aluminum nitride ($\text{Sc}_x\text{Al}_{1-x}\text{N}$), is frequently used in BAW resonators. Due to the piezoelectric effect, these materials are able to change electrical energy into mechanical vibrations and the other way around [7]. Aluminum nitride (AlN) thin films have gained significant attention as the preferred material for BAW resonators due to their exceptional piezoelectric properties and compatibility with integrated circuit technology. However, there is an ongoing need to further enhance the performance of AlN thin films to meet the ever-increasing demands of wireless communication devices. There are two types of AlN based basic BAW resonator architectures that are being used in the resonator industries. One is Thin Film Bulk Acoustic Resonator (FBAR) and the other one is Solidly Mounted Resonator (SMR). The Thin Film Bulk Acoustic Wave Resonator

(FBAR) is positioned above an air cavity, while the Solidly Mounted Resonator (SMR) employs a sequence of high and low impedance reflectors to effectively isolate the resonator from the substrate [8]. This study mainly aims to improve the efficiency of SMR.

1.4 Piezoelectricity

1.4.1 Physics of piezoelectricity

Piezoelectricity refers to the phenomenon wherein specific materials produce an electric charge when subjected to mechanical stress or deformations. The initial observation of piezoelectricity can be attributed to the Curie brothers in the year 1880. They conducted experiments on various materials, including quartz, topaz, and tourmaline, and noted the manifestation of electric charges when subjected to mechanical forces. This phenomenon is commonly referred to as the direct piezoelectric effect. The etymology of the term "piezoelectricity" can be traced back to its Greek origins, where it is derived from the words "piezo" meaning pressure and "electricity". The mathematical derivation of the inverse effect was accomplished by Lippmann in the subsequent year, and its experimental confirmation was promptly conducted by the Curie brothers. The phenomenon of piezoelectricity is commonly observed in various natural occurrences as well as in numerous artificially created materials. Quartz, specifically SiO₂, is widely recognized as the most prominent natural piezoelectric material. In contrast, within the realm of synthetic materials, there exist numerous options, among which ferroelectric ceramics found in solid solutions of lead zirconate and lead titanate ($Pb(Zr, Ti)O_3$), known as PZT, are extensively employed and possess a comprehensive understanding [9]. The unique characteristic of Piezoelectricity arises from the crystalline structure and atomic configuration present in piezoelectric materials. So, to comprehend the principles underlying piezoelectricity, one must take into account the fundamental notions of crystal symmetry, charge distribution, and lattice deformations. Piezoelectric materials are characterized by a crystal structure that is non-centrosymmetric, indicating the absence of an inversion symmetry within their crystal lattice. The materials under consideration exhibit an inherent lack of symmetry in the arrangement of atoms, leading to the emergence of a dipole moment within the unit cell [10]. The varying electronegativities of the atoms that make up a piezoelectric material cause an irregular distribution of positive and negative charges. This unequal charge distribution gives rise to a permanent electric dipole moment within the unit cell. The crystal lattice of a piezoelectric material deforms in response to an applied mechanical stress or strain, which shifts the positive and negative charges inside the unit cell. The dipole moment is changed by this displacement, which also causes the material to produce an electric field or potential across the material. To understand the structural concept better, we can consider the example of Quartz (i.e., SiO₂) showed in Figure 1.1. The simplified configuration of a quartz crystal consist of Silicon (Si) and Oxygen (O₂) atoms

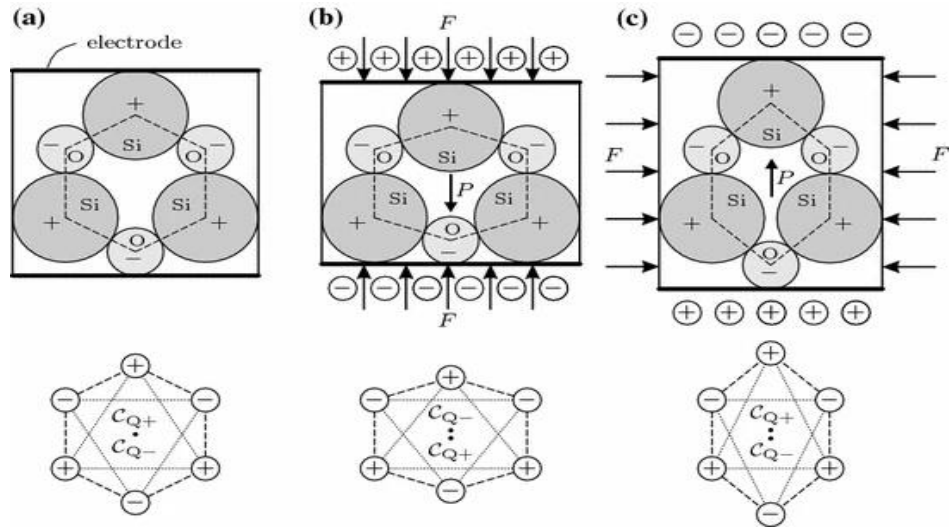


Figure 1.1 A quartz crystal structure with metal electrodes on top and bottom. In a), the crystal is in its initial state, with no mechanical load applied. The longitudinal and transverse piezoelectric effects are depicted in b) and c), respectively. The charge centers, C_{Q+} and C_{Q-} , are also included [11]

entails the presence of metallic electrodes positioned at the upper and lower surfaces. In Fig. 1.1(a), the crystal is in its initial state, devoid of any mechanical load while the longitudinal and transverse piezoelectric effects are portrayed in b) and c), respectively. The mechanical force load F is in two different directions which led to different deformations. The centers of charge, specifically denoted as C_{Q+} and C_{Q-} , are also encompassed within the analysis. As seen, when no force is applied, the geometric center C_{Q+} of positive charges (the Silicon ions) and the center C_{Q-} of negative charges (the Oxygen ions) coincide. As a consequence, the material attains electrical neutrality with respect to its surroundings. Conversely, the application of a mechanical force (F) results in a displacement of the charge centers, causing a deviation from their initial alignment and giving rise to electric dipole moments ranging from C_{Q-} to C_{Q+} . The dipole moment is indicative of the electric polarization denoted as P . In order to rectify this issue, namely an electrical imbalance within the material, charges are induced on the electrodes through electrostatic means. In contrast, the inverse piezoelectric effect occurs when the aforementioned process is reversed, resulting in an electric voltage being applied to the electrodes, thereby inducing charges electrostatically. These charges create an electric imbalance that is counterbalanced by a dipole moment within the material. Figure 1.1(b) illustrates the scenario where the moment aligns with the applied field, known as the longitudinal mode. On the other hand, Figure 1.1(c) depicts the situation where the moment and the applied field are perpendicular to each other, referred to as the transverse mode.

The piezoelectric effect facilitates a linear correlation between mechanical and electrical variables as demonstrated by S. J. Rupitsch [11]. To find the constitutive equations of piezoelectricity, we first start with the linearized state of for the electric flux density D_m and the mechanical strain S_{ij} .

$$dD_m = \varepsilon_{mn}^{T,\theta} dE_n + d_{mkl}^\theta dT_{kl} + \rho_m^T d\theta$$

$$dS_{ij} = d_{ijn}^\theta dE_n + s_{ijkl}^{E,\theta} dT_{kl} + \alpha_{ij}^E d\theta$$

If the temperature change $d\theta$ is neglected (i.e., isothermal change in states), the linearized state equations will become,

$$dD_m = \varepsilon_{mn}^T dE_n + d_{mkl} dT_{kl}$$

$$dS_{ij} = d_{ijn} dE_n + s_{ijkl}^E dT_{kl}$$

with the electric permittivity ε_{mn}^T for constant mechanical stress, the elastic compliance constants s_{ijkl}^E for constant electric field intensity and the piezoelectric strain constants d_{mkl} . Under the assumption that D_m , E_n , S_{ij} as well as T_{kl} are zero in the initial state, the equations can be written as,

$$D_m = \varepsilon_{mn}^T E_n + d_{mkl} T_{kl}$$

$$S_{ij} = d_{ijn} E_n + s_{ijkl}^E T_{kl}$$

These represents the strain-charge form (d-form) of the material law for linear piezoelectricity. Additionally, we can have also the other forms of constitutive equations, i.e., e-form (stress-charge form), g-form (strain-voltage form), and h-form (stress-voltage form). As we'll focus particularly on strain-charge relationship because priority has been given to extract the piezoelectric effect (d_{33}) in this thesis. In this tensor form of strain-charge relation, the first equation is related to direct piezoelectric effect whereas the second equation is related to indirect piezoelectric effect. Due to symmetries within the tensors of rank four for the mechanical field (S_{ijkl}) and the rank of three for piezoelectric coupling (d_{mkl}), the number of the independent components reduce significantly. So, these tensors equations can be transferred into matrix equations. In Voigt notation, the constitutive equations for piezoelectricity (strain-charge) becomes (transpose t),

$$D = [\varepsilon^T]E + [d]T$$

$$S = [d]^t E + [s^E]T$$

The vectors representing the electrical field (D, E) are characterized by three components, whereas the vectors representing the mechanical field (T, S) exhibit six independent components. The reduced set of constitutive equations for piezoelectricity in d-form, expressed in component notation is given by,

$$\begin{bmatrix} D_1 \\ D_2 \\ D_3 \end{bmatrix} = \begin{bmatrix} \varepsilon_{11}^T & \varepsilon_{12}^T & \varepsilon_{13}^T \\ \varepsilon_{21}^T & \varepsilon_{22}^T & \varepsilon_{23}^T \\ \varepsilon_{31}^T & \varepsilon_{32}^T & \varepsilon_{33}^T \end{bmatrix} \begin{bmatrix} E_1 \\ E_2 \\ E_3 \end{bmatrix} + \begin{bmatrix} d_{11} & d_{12} & d_{13} & d_{14} & d_{15} & d_{16} \\ d_{21} & d_{22} & d_{23} & d_{24} & d_{25} & d_{26} \\ d_{31} & d_{32} & d_{33} & d_{34} & d_{35} & d_{36} \end{bmatrix} \begin{bmatrix} T_1 \\ T_2 \\ T_3 \\ T_4 \\ T_5 \\ T_6 \end{bmatrix}$$

$$\begin{bmatrix} S_1 \\ S_2 \\ S_3 \\ S_4 \\ S_5 \\ S_6 \end{bmatrix} = \begin{bmatrix} d_{11} & d_{21} & d_{31} \\ d_{12} & d_{22} & d_{32} \\ d_{13} & d_{23} & d_{33} \\ d_{14} & d_{24} & d_{34} \\ d_{15} & d_{25} & d_{35} \\ d_{16} & d_{26} & d_{36} \end{bmatrix} \begin{bmatrix} E_1 \\ E_2 \\ E_3 \end{bmatrix} + \begin{bmatrix} s_{11}^E & s_{12}^E & s_{13}^E & s_{14}^E & s_{15}^E & s_{16}^E \\ s_{21}^E & s_{22}^E & s_{23}^E & s_{24}^E & s_{25}^E & s_{26}^E \\ s_{31}^E & s_{32}^E & s_{33}^E & s_{34}^E & s_{35}^E & s_{36}^E \\ s_{41}^E & s_{42}^E & s_{43}^E & s_{44}^E & s_{45}^E & s_{46}^E \\ s_{51}^E & s_{52}^E & s_{53}^E & s_{54}^E & s_{55}^E & s_{56}^E \\ s_{61}^E & s_{62}^E & s_{63}^E & s_{64}^E & s_{65}^E & s_{66}^E \end{bmatrix} \begin{bmatrix} T_1 \\ T_2 \\ T_3 \\ T_4 \\ T_5 \\ T_6 \end{bmatrix}$$

For $Sc_xAl_{1-x}N$, because of its crystal symmetry, the number of independent components is considerably reduced to the form stated below.

$$\begin{bmatrix} D_1 \\ D_2 \\ D_3 \end{bmatrix} = \begin{bmatrix} \varepsilon_{11}^T & 0 & 0 \\ 0 & \varepsilon_{11}^T & 0 \\ 0 & 0 & \varepsilon_{33}^T \end{bmatrix} \begin{bmatrix} E_1 \\ E_2 \\ E_3 \end{bmatrix} + \begin{bmatrix} 0 & 0 & 0 & 0 & d_{15} & 0 \\ 0 & 0 & 0 & d_{15} & 0 & 0 \\ d_{31} & d_{31} & d_{33} & 0 & 0 & 0 \end{bmatrix} \begin{bmatrix} T_1 \\ T_2 \\ T_3 \\ T_4 \\ T_5 \\ T_6 \end{bmatrix}$$

$$\begin{bmatrix} S_1 \\ S_2 \\ S_3 \\ S_4 \\ S_5 \\ S_6 \end{bmatrix} = \begin{bmatrix} 0 & 0 & d_{31} \\ 0 & 0 & d_{31} \\ 0 & 0 & d_{33} \\ 0 & d_{15} & 0 \\ d_{15} & 0 & 0 \\ 0 & 0 & 0 \end{bmatrix} \begin{bmatrix} E_1 \\ E_2 \\ E_3 \end{bmatrix} + \begin{bmatrix} s_{11}^E & s_{12}^E & s_{13}^E & 0 & 0 & 0 \\ s_{12}^E & s_{11}^E & s_{13}^E & 0 & 0 & 0 \\ s_{13}^E & s_{13}^E & s_{33}^E & 0^E & 0 & 0 \\ 0 & 0 & 0 & s_{44}^E & 0 & 0 \\ 0 & 0 & 0 & 0 & s_{44}^E & 0 \\ 0^E & 0 & 0 & 0 & 0 & \frac{s_{11}^E + s_{22}^E}{2} \end{bmatrix} \begin{bmatrix} T_1 \\ T_2 \\ T_3 \\ T_4 \\ T_5 \\ T_6 \end{bmatrix}$$

1.4.2 Electromechanical coupling factor

Electromechanical coupling factors, denoted as k_t , are frequently employed to assess the efficiency of energy conversion in piezoelectric materials. This pertains to the process of transforming mechanical energy into electrical energy, as well as converting electrical energy into mechanical energy. These conversions are represented by the equations ($1 \leq i \leq 3$; $1 \leq p \leq 6$). As mentioned earlier, piezoelectricity is a phenomenon that establishes a connection between the electrical and mechanical domains. However, in a piezoelectric material, the conversion of mechanical energy to

electrical energy, and vice versa, is not complete. The parameter k_t^2 , which represents the electromechanical coupling, serves as a measure of the effectiveness of the conversion process. It is defined as,

$$k_t^2 = \frac{\text{mechanical energy converted into electrical energy}}{\text{mechanical input energy}}$$

Or,

$$k_t^2 = \frac{\text{electrical energy converted into mechanical energy}}{\text{electrical input energy}}$$

As evidenced by the findings in reference [11], the electromechanical couplings exhibit equivalence in both conversion directions, consistently maintaining a value below 1.

1.4.3 Piezoelectric materials

Piezoelectric materials demonstrate a crystal structure or, at the very least, regions characterized by a crystal-like arrangement. In a broad sense, a crystal is distinguished by the presence of a regularly recurring atomic lattice structure that extends uniformly in all spatial dimensions. The fundamental repeating unit of a crystal is referred to as the unit cell. The identification of crystal classes, also known as crystallographic point groups, is based on the symmetry properties exhibited by the unit cell. This classification system yields a total of 32 distinct crystal classes. Among them, 11 are centrosymmetric and 21 are non-centrosymmetric. Piezoelectric properties show up exclusively in the presence of structural asymmetry within the unit cell. Except for 432, where all the value of $d_{ij} = 0$, all classes of non-centrosymmetric crystals are piezoelectric. Because of symmetry relationships, certain d in the higher classes become zero, equal to others, identical in magnitude but opposite in sign, or doubled in magnitude which counts 20 among 21 non-centrosymmetric crystal structure. Among the piezoelectric crystal group, 10 crystal classes are pyroelectric and the remaining 10 are non-pyroelectric. The material tensors, exhibit variations among piezoelectric materials based on their crystal classes. These variations are observed in terms of the number of independent material parameters and the presence of nonzero entries.

1.5 Ferroelectricity

1.5.1 Introduction to ferroelectricity

Sc-doped Aluminum Nitride ($ScAlN$), the focus of the current investigation, was recently found to be ferroelectric [12]. Among the 20 piezoelectric crystal point group mentioned in section 1.6, 10-point groups are characterized by a distinct polar axis, enabling them to exhibit a spontaneous polarization P_s despite the absence of an external electric field. These types of materials are commonly referred to as ferroelectrics. Due to the vector nature of polarization, which implies the presence of an orientation, ferroelectric materials exhibit a minimum of two equilibrium

orientations for their spontaneous polarization. These materials have the ability to switch between states in the presence of external electric field. The stability of these polarization states led to the adoption of the term "ferroelectricity," drawing an analogy to the phenomenon of ferromagnetism. The manifestation of ferroelectric properties typically relies on the temperature conditions. These materials experience a phase transition wherein they change from a phase characterized by low temperature and low symmetry to a phase characterized by high temperature and higher symmetry. Alternatively, the transition between states might occur in the opposite direction, depending on the temperature [13]. The temperature at which the ferroelectric phase changes into the non-ferroelectric (or paraelectric) phase is called the Curie Temperature (T_c). It distinguishes the ferroelectric and non-ferroelectric (or paraelectric) phases. The dielectric constant of materials decreases when they are subjected to a temperature above the Curie Temperature [14]. Based on the Curie-Weiss law,

$$\varepsilon = \varepsilon_0 + \frac{C}{T - T_0}$$

where C is the constant of Curie and T_0 is the temperature of Curie-Weiss. A few ferroelectrics like barium titanate experience multiple phase transitions. In polycrystalline ferroelectric materials, spontaneous polarization is not uniform. In some places, the net polarization vector points in a different direction than in others. Domain walls divide domains. In the ferroelectric, spontaneous polarization produces a surface charge and an imbalance. This imbalance generates the depolarizing field E_d , which is oriented opposite P_s . Domains are formed in order to reduce depolarizing field electrostatic energy. When E_d is high (MV/cm^2), the single domain state is energetically unfavorable. When nearby domains have opposite polarization, energy is decreased. Mechanical stress has the ability to break ferroelectric domains.

Real materials are divided into several domains because to the complex mechanical and electrical boundary conditions of each grain. This action may cancel out net polarization across the material, resulting in the disappearance of piezoelectric and ferroelectric capabilities. Poled materials have non-zero polarization and domains which can be reoriented under external field. High-temperature electric fields are used in the poling process. Figure 1.2 depicts poling in a polycrystalline ferroelectric, although it can be also produced in a single-domain crystal. A single domain state can be obtained by poling of polycrystals.

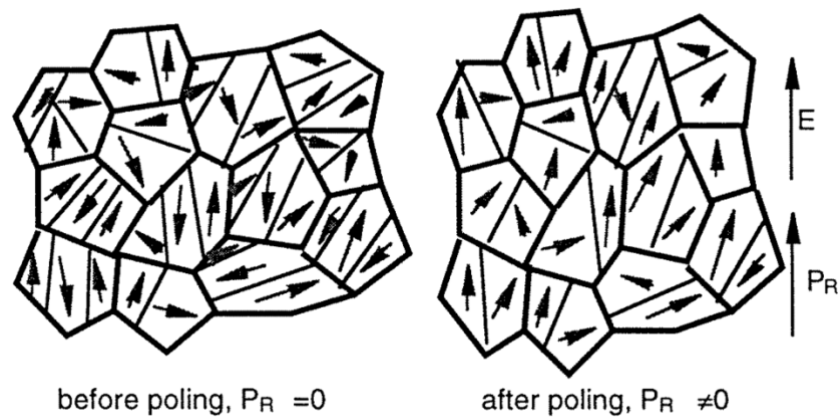


Figure 1.2 A polycrystalline ferroelectric with grains that are randomly oriented before and after poling [14]

From the figure, we can see that, despite the presence of numerous domain walls within the polycrystalline structure, the remanent polarization is not equivalent to zero. If the polarization remains non-zero even after the removal of the applied field ($E = 0$), it is called the remanent polarization (P_r). The highest possible level of the remanent polarization obtainable in a polycrystalline material is dependent upon the range of domain states that are accessible. As example, in a tetragonal ferroelectric crystalline structure, with six available domain states, the maximum remanent polarization $(P_r)_{max} = 0.87P_S$ and in rhombohedral ferroelectric structure which possesses eight distinct domain states, the remanent polarization $(P_r)_{max} = 0.87P_S$ [15]. Nevertheless, a polycrystalline ferroelectric material with a poled structure has both pyroelectric and piezoelectric characteristics, despite the presence of several domain barriers.

1.5.2 Ferroelectric hysteresis loop

The primary attribute of ferroelectric materials that holds significant importance is the phenomenon of polarization reversal, also known as switching, induced by an electric field. It is mentioned earlier that ferroelectric material has two stable states of polarization. The experimental observation of the hysteresis loop can be achieved by utilizing the Sawyer-Tower approach, which involves the switching between two polarization states under the influence of an external electric field [16]. At small value of electric field applied, the polarization increases linearly with the field amplitude although the applied field alone may not be sufficient to induce a transition in domains with an unfavorable polarization orientation. If we increase the electric field, all the domain indifferent of favorable and unfavorable polarization direction will start to switch the direction of polarization according to the applied field direction. The charge density will exhibit a quick increase as well. The level of polarization observed in this particular location has a highly non-linear behavior. When the applied field is enough to change the polarization direction of all the domains in the ferroelectric material, the change in polarization again becomes linear and the ferroelectricity occurs. If we start

to decrease the field intensity, the polarization in some domains will also begin to change the direction as well as the ferroelectricity starts to decrease. However, when the applied field the zero, the polarization will not turn in neutral. There will be some positive ferroelectricity even if the applied field is zero. To reach zero polarization, we need to switch the direction of the electric field. Increase the electric field strength in the negative direction will occur more domain to back-switching. Hence at some point, the polarization will become zero. If the field strength is continued to increase in this direction, the polarization direction will become altered, and we will see the other polarization state. As the field increases, the polarization will become nonlinear again and saturates like before but in the opposite direction. Again, if we alter the direction of the electric field, some domains will start back switching the direction and the polarization will start to decrease. If the applied field reversed to zero to complete the cycle, there will be remaining polarization like before, a nonzero value. The polarization that remains in the absence of an external field is referred to as the remanent polarization, denoted as P_R . In order to cancel out the polarization, it is important to apply additional field in a positive direction. The field required to reduce the polarization to zero is commonly referred to as the coercive field, denoted as E_C . The phenomenon of spontaneous polarization. The parameter P_S is commonly regarded as the point at which the polarizing axis intersects the extended linear region. However, it should be noted that in polycrystalline structures, the spontaneous polarization does not achieve the same level as in single crystalline structures. The coercive field E_R , as determined through the intersection of the hysteresis loop, does not correspond to the threshold field [17]. Figure 1.3 represents the hysteresis loop of a ferroelectric material.

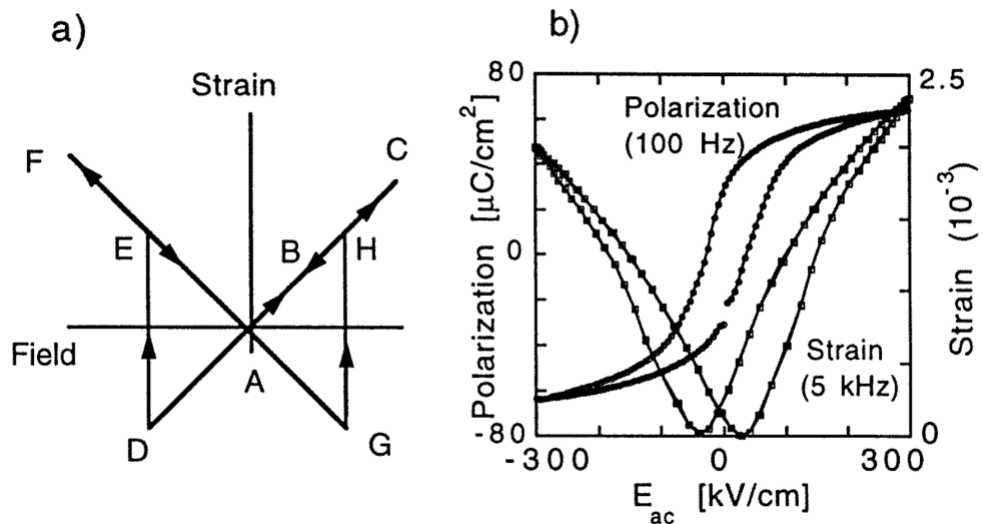


Figure 1.3 Strain–electric field (x–E) hysteresis loop (butterfly loop) in ferroelectrics: (a) idealized loop in a crystal where polarization changes by only 180° , and (b) real polarization and strain loops measured on (111)-oriented, 322 nm thick, sol-gel $Pb(Zr_{0.53}Ti_{0.47})O_3$ thin film [14].

Furthermore, the alteration of polarization in ferroelectric materials due to an electric field also induces a strain-electric field hysteresis, as seen in Figure 1.3. The presence of the hysteresis loop in the strain-electric field relationship can be attributed to three distinct types of effects. There are three distinct mechanisms that contribute to the observed phenomena: the conventional reverse piezoelectric effect of the lattice, as well as the switching and movement of domain walls. For illustrative purposes, we will use a mono-domain single crystal of $PbTiO_3$, whereby the polarization is hypothetically capable of instantaneous alteration by 180° . The next elucidation provides a concise yet informative account of how the strain of the crystal undergoes alterations in response to variations in the applied field.

A At the location denoted as point A in Figure 11(a), where the absence of a field is observed, it is postulated that the crystal exhibits a state of strainlessness. The electric field is subsequently administered in a manner analogous to the spontaneous polarization. As the field intensifies, the piezoelectric action induces crystal growth, resulting in an expansion in size, while the pressure exhibits a linear progression along the A-B-C trajectory. The field gradually expands until it reaches point C, at which it attains its maximum size. At point C, the field exhibits a reduction in size, while maintaining its parallel alignment with P_S . The strain exhibited by the sample demonstrates a reverse progression, moving from C to A. At point A, the force returns to a state of equilibrium. The field subsequently changes its direction, moving in the opposite direction to that of P_S . As the magnitude of the field strength increases in the negative direction, the crystal exhibits a displacement away from point A. At point D, the magnitude of the field is sufficiently significant to induce a modification in the trajectory of the division process. Upon transitioning, the polarization aligns itself with the electric field, resulting in the strain returning to a positive state (referred to as point E). As the magnitude of the field intensifies in the negative direction, the strain correspondingly increases till reaching point F. When the magnetic field weakens, the strain returns to point A. At location G, the polarization undergoes a reversal in the opposite direction, leading to a rapid alteration in pressure. The strain-field curve has a linear relationship, indicating that the majority of the strain is attributed to the piezoelectric effect, with the exception of points D and G where it undergoes alterations. The relationship between strain and field is more intricate in practice, as seen in figure 11(b) for a thin layer of $Pb(Zr_{0.53}Ti_{0.47})O_3$. The majority of ceramic samples have many domains that deviate from a 180° -degree orientation. In conjunction with the inherent piezoelectric response exhibited by the material within each domain, the displacement and transition of walls that are not oriented at a 180° -degree angle can give rise to a substantial alteration in the dimensions of the specimen. This phenomenon arises due to the variation in coercive field across different regions, resulting in a less abrupt polarization reorientation in actual materials compared to the idealized depiction illustrated in figure 11(a). During the process of field cycling, it is possible to see a residual strain, also known as remanent strain, at the zero-field level if the domains fail to revert to their initial positions [18][19]. The attainment of the single-domain condition in several experiments

sometimes necessitates the use of exceedingly strong magnetic fields. This implies that the portion of the strain-field connection that is saturated, non-hysteretic, and linear may not be observable. Conversely, the displacement of domain walls exhibits a pronounced nonlinearity and hysteresis in its impact on the strain. This phenomenon, which is frequently observed in experimental settings, pertains to the relationship involving strain and electric field.

Chapter 2: Deposition techniques

2.1 Magnetron sputtering

Within the area of the study of materials, the capacity to manipulate the characteristics of thin films holds utmost significance in the advancement of state-of-the-art technologies. Magnetron sputtering is widely recognized as a highly versatile and precise method utilized for the deposition of thin films. The aforementioned procedure has brought about a significant transformation in various sectors, including electronics, optics, energy, and aerospace. It has achieved this by facilitating the production of customized thin films of exceptional quality, while also granting exceptional command over their composition, thickness, and properties. The Magnetron sputtering process was employed for the deposition of the thin film ($\text{Sc}_x\text{Al}_{(1-x)}\text{N}$). Magnetron sputtering is a type of physical vapor deposition (PVD), which is a group of methods used to make thin films by condensing vaporized material on a substrate. In contrast to conventional deposition techniques, magnetron sputtering utilizes plasma, a state of matter characterized by charged particles, to convert solid target materials into vapor and subsequently deposit them onto the substrate. The focal point of this methodology revolves around the magnetron sputtering source, which encompasses a cathode equipped with potent magnets positioned at the rear of the target substance. The magnetron effect, a magnetic configuration, effectively confines electrons in close proximity to the surface of the target, thereby increasing ionization and improving the efficiency of the sputtering process. The procedure takes place within a controlled environment known as a vacuum chamber, wherein a process gas, typically an inert noble gas such as argon, is introduced. Upon the application of a high voltage to the target material, the gas undergoes ionization, resulting in the formation of a plasma consisting of positively charged ions and electrons. Subsequently, the ions undergo acceleration towards the surface of the target, possessing kinetic energy that, upon collision, results in the displacement of atoms within the target. The atoms undergo transmutation, transforming into vapor and subsequently traversing the vacuum chamber. Eventually, they condense onto a substrate, resulting in the formation of a thin film layer. Bendjerad et al. also showed similar magnetron co-sputtering system for their deposition process in their publication along with the process illustration [20]. The schematic of magnetron sputtering deposition technique operated in Evatec CLUSTERLINE system is shown in Fig 2.1.

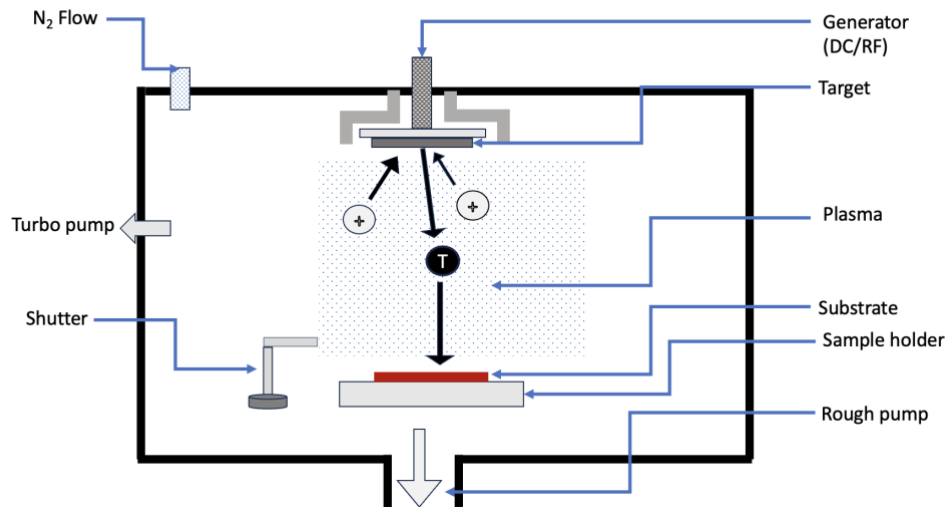


Figure 2.1 Schematic illustration of magnetron sputtering system.

The sputtering process has gained significant momentum in thin film deposition technology due to its notable attributes. The remarkable precision and meticulous control exhibited by this technique have instigated a paradigm shift in the realm of thin film fabrication. The regulation of sputtering power, gas pressure, and target-substrate distance by scientists and engineers effectively governs the qualities of films. The fabrication of tailored materials can be accomplished by finely tuning parameters such as thickness, composition, and morphology. Magnetron sputtering is a highly adaptable deposition technique that demonstrates the capability to process a diverse array of materials, encompassing metals, semiconductors, insulators, and dielectrics. The presence of reactive gases and the inherent flexibility of the process facilitate the synthesis of oxides and nitrides. This enables the advancement of versatile material systems suitable for a diverse array of applications. The effectiveness of magnetron sputtering can be attributed to its inherent property of homogeneity. The microelectronics and optics industries heavily depend on the existence of homogeneous films that uniformly cover large substrate surfaces. Magnetron sputtering is a highly advantageous technique for depositing materials onto substrates that are sensitive to temperature, primarily due to its inherent low-temperature characteristics. This specific attribute facilitates the incorporation of thin films in a wider array of applications within the realm of materials science. Furthermore, magnetron sputtering is widely recognized as the predominant technique employed in the industrial sector. The technology mentioned above plays a crucial role in the production of semiconductors in the microelectronics industry, particularly in the manufacturing of integrated circuits that are widely used in modern computer systems. Additionally, the utilization of anti-reflection and reflective coatings significantly improves the optical capabilities of lenses, mirrors, and displays. Protective and thermal barrier coatings find application in the aerospace industry, whereas efficient thin film solar cells are employed in the domain of renewable energy.

Because of these exceptional benefits, we used a Magnetron co-sputtering process handler called Evatec CLUSTERLINE® 200 for our deposition process.

2.2 Evatec CLUSTERLINE® 200 magnetron co-sputtering system

The CLUSTERLINE® 200 has the capability to be adapted for either single substrate or batch processing through the utilization of Single Process Modules (SPM) or a Batch Process Module (BPM) correspondingly. Regardless of the configuration of the tool, it can be confidently relied upon for fully automated cassette-to-cassette processing, employing Evatec's established safe handling practices. In order to accommodate custom applications, it is necessary to employ configurations that integrate both single and batch process modules. According to the Evatec CLUSTERLINE® 200 product details from the company website [21], the utilization of SPM configuration is imperative for platforms that possess a robust lineage in Power Devices, Advanced Packaging, MEMS, and Wireless markets. This configuration facilitates effortless tool customization and enables future scalability for various processes such as PVD, highly ionized PVD, Soft Etch, PECVD, and PEALD, specifically designed for wafer sizes up to 200mm. The modular chuck is specifically engineered to facilitate swift interchangeability between 100, 150, or 200mm formats, thereby enhancing production flexibility and optimizing tool utilization. There exists a maximum of six individual process modules, as well as an additional six auxiliary modules, which are utilized for pre and post treatment procedures. The auxiliary module encompasses several essential functions, such as wafer alignment, buffer, degas, cooling, and ID reader. This study aims to develop a specialized capability for the direct handling and processing of thin wafers with thicknesses as low as 70 microns. In context of BPM configuration, various platforms exhibit differences in their ability to integrate the advantages of sputter batch processing with fully automated handling, specifically for targeted applications within the fields of MEMS and Wireless technology. The device is widely recognized for its exceptional performance and reliability in the fields of LED/Micro Display and Photonics industries. The incorporation of supplementary plasma sources expands the range of potential applications for deposition processes, such as the modification of coatings through techniques like gap filling and planarization. The batch processing capability of this system allows for the simultaneous rotation of up to 21 substrates, which can be either 4 inches or 8 inches in size. The substrate table provides the option for individual rotation of the substrate chucks. The PM chamber is equipped with the capability to integrate a maximum of four physical vapor deposition (PVD) sputter sources, in addition to one plasma source. The CLUSTERLINE system installed in the laboratory incorporates two process module chambers for conducting experiments. The Process Module (PM) - 6 is utilized for single clustered target source applications, while the Process Module (PM) - 1 is employed for co-sputtering of multi target sources. Due to the necessity of doping Scandium with Aluminum and Nitrogen, we have relied heavily on PM1 for sputtering our preferred film deposition. There exist two load-locks, denoted as A and B, which have the capacity to accommodate 21 and 16 wafers, respectively. These wafers possess diameters of up to 200mm. The process module is equipped with four pulsed direct current (DC) generators, and a radio frequency (RF) bias power source, which are integrated into its design.

2.3 Deposition of $Sc_xAl_{1-x}N$ film

In this study, the deposition of $Sc_xAl_{1-x}N$ was conducted on a Silicon (Si) (100) wafer with a diameter of 200 mm and a width of 725 μm . The deposition condition and properties are influenced by various parameters, including temperature, pressure, gas flow rate, and chuck height. Various doping levels ($x = 0.10$ to 0.50) of Scandium have been incorporated into Aluminum Nitride. The scandium doping rate was determined through the utilization of the Energy Dispersive X-Ray Spectroscopy (EDX) technique. Following the determination of the relative ratio between power and doping rate, various pulsed DC power levels were employed on the Scandium (Sc) target to achieve different concentrations through sputtering. Meanwhile, the power of the Aluminum DC generator remained constant. Table 2.1 presents the relationship between the Sc power and doping concentration.

Table 2.1 Scandium doping rate to generator power comparison

Scandium (Sc) doping percentage (%)	Sc pDC Power (W)	Al pDC Power (W)	N_2 Flow (SCCM)	Chuck Height (nm)	Thickness (nm)	Temperature ($^{\circ}C$)
10	125	950	30	30	500	450
20	275					
30	480					
35	600					
40	720					
45	850	20				

By referring to Table 2.1, insights can be gained regarding the correlation between the power of the Scandium target generator and the doping rate. The deposition of this batch occurred at a temperature of 450 $^{\circ}C$, while the base pressure of process module-1 (PM-1) was approximately within the range of 10 $^{-7}$ to 10 $^{-8}$ mbar. In order to determine the optimal temperature, N_2 flow rate, and chuck height (i.e., the distance between the substrate and target), a series of depositions were conducted on a silicon wafer using various parameters. Table 2.2 presents a comprehensive overview of the preceding depositions, highlighting variations in temperature, N_2 flow, and chuck height compositions.

Table 2.2 Comparative analysis among Temperature, Chuck height and N₂ Flow

Wafer label	Chuck T [C]	Distance [mm]	N2 flow [sccm]	Thickness [nm]	Stress [MPa]	RC	Targeted Sc [%]
A1	450	20	20	262	-779	2.25	30
A2	450	20	30	233	-242	2.25	
A3	450	30	30	223	-12	2.33	
A4	450	30	20	256	-662	2.33	
A5	350	20	20	264	-957	2.38	
A6	350	20	30	234	-744	2.23	
A7	350	30	20	257	-856	2.28	
A8	350	30	30	224	-188	2.34	
A9	450	20	20	320	-1255	1.86	40
A10	450	20	30	277	-499	1.9	
A11	450	30	30	306	-1173	1.87	
A12	450	30	20	264	-447	2	
A13	350	20	20	316	-1428	1.87	
A14	350	20	30	276	-658	1.86	
A15	350	30	20	307	-1367	1.95	
A16	350	30	30	265	-607	1.95	

Based on the comparative analysis presented in Table 2.2, the temperature of 450°C was determined to be the optimal condition for the deposition of our film. The decision to use the particular sample was influenced by the fact that, when subjected to a temperature of 450°C, the film displayed enhanced levels of crystallinity. The determination of the film's crystallinity can be inferred through analysis of the Rocking Curve (RC) obtained via the X-Ray Diffraction (XRD) technique. The stress levels were quantified using the Tensor Flex thin film stress measurement machine. The method precisely quantifies alterations in the substrate's radius of curvature resulting from the application of a stressed thin film onto the substrate. Furthermore, an Ellipsometer was employed to ascertain the thickness of the film. The technique of ellipsometry quantifies alterations in polarization that occur when light interacts with a material

structure, either through reflection or transmission. The magnitude of the response is contingent upon the thickness of each respective material. After conducting a thorough analysis of stress and crystallinity factors, we have determined that a temperature of 450°C, along with a fixed distance of 30 mm from the substrate to the target (referred to as chuck height), is the optimal condition for our subsequent deposition processes. In the case of N₂ flow rate, a value of 30 sccm was determined to be optimal for Sc doping levels below 40%. Conversely, for Sc doping levels exceeding 40%, a fixed N₂ flow rate of 20 sccm was deemed the most appropriate approach for subsequent deposition processes. Based on the comparative analysis presented in Table 2.2, the optimal deposition parameters were identified. The subsequent course of action involves the deposition of our most exemplary recipes in order to characterize the film properties, thereby enhancing our understanding of the impact of Scandium doping in Aluminum Nitride films.

2.4 Detecting the doping level of Scandium

Regarding the actual percentage of scandium (Sc) doping in aluminum nitride (AlN), we used a SUPRA-25 Scanning Electron Microscope (SEM) in conjunction with Energy Dispersive X-Ray Spectroscopy (EDS). The SUPRA-25 Field Emission Scanning Electron Microscopy (FESEM) utilizes a unique GEMINI field emission column in order to achieve remarkable resolution at the nanometer level across a wide range of accelerating voltages, ranging from 100 electron volts (eV) to 30 kiloelectron volts (KeV). A voltage of 20 kilovolts (20 kV) was employed for the EDS analysis. The QUANTAX Microanalysis system, manufactured by Bruker Corporation, was employed for the EDS measurement. The obtained measurement data from the EDS system is consistent with previous studies where the films were deposited using the Evatec CLUSTERLINE magnetron co-sputtering system, as reported in the literature. In their study, R. Beaucejour et al. utilized a sputtering system identical to ours and conducted a comparative analysis of the doping percentage of Scandium (Sc) with respect to the power level of the Sc target generator [22]. In their study, the authors documented a Sc doping level of 20.3% at a pulsed DC (pDC) generator power of 300 W. In contrast, our findings revealed a Sc doping level of 20.2% at a pDC power of 275 W. Nevertheless, the aforementioned study documented a doping percentage of 34.5% for Scandium (Sc) at a power level of 605 W. In contrast, our experimental results yielded a doping percentage of 34% for Scandium at a lower power level of 480 W. The variation in doping rate with respect to power level may be attributed to the influence of additional control parameters. As an example, the film was subjected to a deposition process at a temperature of 450°C, utilizing a nitrogen flow rate of 30 standard cubic centimeters per minute (sccm) and a chuck height of 30 millimeters. In contrast, their film deposition was conducted at a temperature of 350°C, employing a nitrogen flow rate of 20sccm, and the specific chuck height utilized remains undisclosed. Although the deposition technique remained the same, there were variations in the controlling parameters. Therefore, it is impossible to eliminate any potential correlations between the power of the target generator and the doping rate of scandium. Table 2.3 presents the correlation between the power of the scandium target generator and the

measured scandium doping rate using Energy Dispersive Spectroscopy (EDS) in our deposition methodology.

Table 2.3 Detection of Scandium doping rate

Sample name	Target Sc%	Actual Sc% measured in EDS	Sc target generator power (pDC) in W
T6	10	7.8	125
T8	20	20.2	275
T10	30	34	480
T12	40	43	720

Throughout all of the depositions, the power of the Aluminum (Al) target generator remained constant at 900W pDC + 100 W RF. The experimental setup maintained a constant distance of 30nm between the target and substrate during the deposition process, resulting in a deposition of up to 30% Sc. However, for a deposition of 40%, the distance was reduced to 20nm. The flow rate of N₂ was set at a constant value of 30 standard cubic centimeters per minute (scm), while the temperature was maintained at 450°C. The deposition control parameters were adjusted in order to effectively evaluate the quality of the film in future deposition processes.

2.5 Realizing deposition rate of $Sc_xAl_{1-x}N$ thin films

For the entire experiment, quantifying the $Sc_xAl_{1-x}N$ deposition rate was essential because we wanted to deploy a nanometer scale thin layer of $Sc_xAl_{1-x}N$ over a 750 μm thick Silicon (Si) wafer. The amount of time required for the deposition of a particular thickness was determined, and as a result, the deposition rate of $Sc_xAl_{1-x}N$ thin layer later over Si substrate was computed. In order to determine the deposition rate, we conducted a series of experiments involving the deposition of samples with varying thicknesses in a controlled environment. Specifically, the deposition controlling parameters remained consistent across all of these deposition processes. We fabricated thin films of $Sc_xAl_{1-x}N$ with nominal thicknesses of 200nm, 300nm, and 500nm, respectively. The thickness of these films was measured using a Woollam ESM-300 Ellipsometer. Ellipsometry is a scientific method employed to quantify the polarization of light as it interacts with or traverses a material structure. The amplitude ratio and phase difference are indicative of the extent of polarization change. The determination of very thin film thickness can be achieved by considering the dependence of the polarization response on film thickness and refractive indices. The J.A. Woollam ESM-300 is a spectroscopic ellipsometer capable of measuring thin layer thicknesses as small as 1nm. The ellipsometer used in this study has a spectral range of 245 – 1690 nm, corresponding to 660 wavelengths. The angle of incidence for the

measurements varied between 20° and 90° [23]. A series of samples with varying thicknesses were deposited in order to investigate potential discrepancies in the deposition rate of $Sc_xAl_{1-x}N$. The actual thickness of each sample was measured using an ellipsometer, revealing minor variations in the deposition rate within a comparable deposition environment. The potential sources of disruption in the continuous current supply to the generators could be attributed to measurement errors or electrical issues. Additionally, the deposition rate exhibits variation for different levels of Scandium doping. After conducting a thorough analysis, we have chosen specific average deposition times for the $Sc_xAl_{1-x}N$ layer with a selected thickness. Subsequently, we have computed the deposition rates for various doping levels of scandium. We set a target thickness of 500 nm for our final deposition in order to characterize the thin layer. The average deposition time for the thin film of $Sc_xAl_{1-x}N$ with a thickness of 500nm was determined after a careful consideration. Figure 2.2 illustrates the graphical representation of the deposition rate of $Sc_xAl_{1-x}N$ as a function of varying levels of scandium doping.

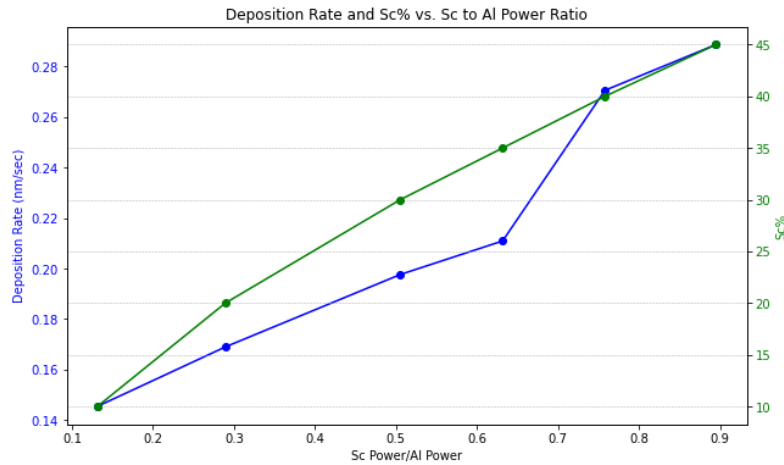


Figure 2.2 Sc doping percentage and $ScAlN$ deposition rate correlation with Scandium to Aluminum power ratio

The graphical representation of Fig. 2.2 clearly shows that $Sc_xAl_{1-x}N$ deposition rate and the scandium to aluminum generator power ratio are highly correlated. Though there are some fluctuations from the median line, the deviation is not that great. Though the median line has not been indicated, at higher fraction of Sc to Al generator power ratio, the deposition rate increases a bit from the normal path. It can be clearly depicted that the deposition rate increases with the Sc% increasing order. Upon completion of the calculation of the deposition rate for the $Sc_xAl_{1-x}N$ material, we proceeded to deposit the film in order to conduct the final measurement. Table 2.4 illustrates the recorded deposition time alongside the corresponding thickness measurements for each individual sample.

Table 2.4 Recorded thickness data with deposition time and Sc to Al generator power ratio.

Sample label	Sc%	Deposition Time	Measured Thickness	Sc Power	Al Power	Sc to Al Power Ratio
U1	10	3190	464	125	950	0.131578947
U2	20	3071	519	275	950	0.289473684
T20	30	2722	538	480	950	0.505263158
T21	35	2285	482	600	950	0.631578947
T22	40	1870	506	720	950	0.757894737
T23	45	1500	433	850	950	0.894736842

Chapter 3: Characterization of $Sc_xAl_{1-x}N$ thin films

3.1 Stress measurement

After the deposition of the $Sc_xAl_{1-x}N$ thin film at optimum environment, the first characterization step was to measure the stress on the substrate. For this measurement we used KLA-Tencor's FLX-2320 thin film stress measurement system. This FLX-2320 system integrates a dual wavelength technology allows the system to determine the optimal wavelength for a specific application. The ideal wavelength is chosen in advance to reduce destructive interference patterns from transparent coatings such as silicon nitride [24]. Furthermore, the laser assembly has only one moving component, resulting in low vibration and good accuracy. The FLX-2320-S computes stress by measuring the difference in film curvature before and after deposition. The stress in a system can be calculated using Stoney's equation, which takes into account several factors including the biaxial modulus of the substrate, the thickness of both the film and substrate, and the difference between the radii of curvature before and after the process. The curvature of a surface can be determined by directing a laser at the surface with a known spatial angle. The position-sensitive photodiode is subjected to illumination from the reflected beam. The process of employing surface scanning techniques is utilized to capture the geometric properties of the film. As premeasurement of radius of the wafer curvature is needed, we measured it and recorded in the computer memory attached to the system. The FLX-2320 device is equipped with two solid-state lasers. The first laser is classified as Class IIIA and emits a power of 4mW at a wavelength of 670nm. The second laser is classified as Class IIIB and emits a power of 4mW at a wavelength of 750nm [25]. Though we used 8" wafer which is the standard sample size for the machine holder, this system also offers extra substrate holder to measure 4" wafers. The only limitation this system has except the wafer size restriction, the substrates have to be reflective as this machine uses the reflection property of laser light to measure the stress of films.

The samples we deposited for the detailed characterization were measured again after deposition and the system computer matched the premeasurement data that were recorded earlier. From the difference, it gave us the film stress. Figure 3.1 express the dependency of film stresses on Sc doping level in AlN film. From the chart it can be clearly depicted that the film stress strongly depends on the scandium doping level. As mentioned previously, the Sc to Al power ratio is highly correlated with the Sc doping percentage, we can use Sc% in writing instead of Sc to Al power ratio. Though there was a change of N_2 supply from 30sccm to 20sccm for 40% and 45% of Sc doping, it should not affect too much for the stress variation. Other deposition parameters were constant for all of the samples. The transition of film stresses from tensile to compressive is remarkable with the increase of Sc doping level.

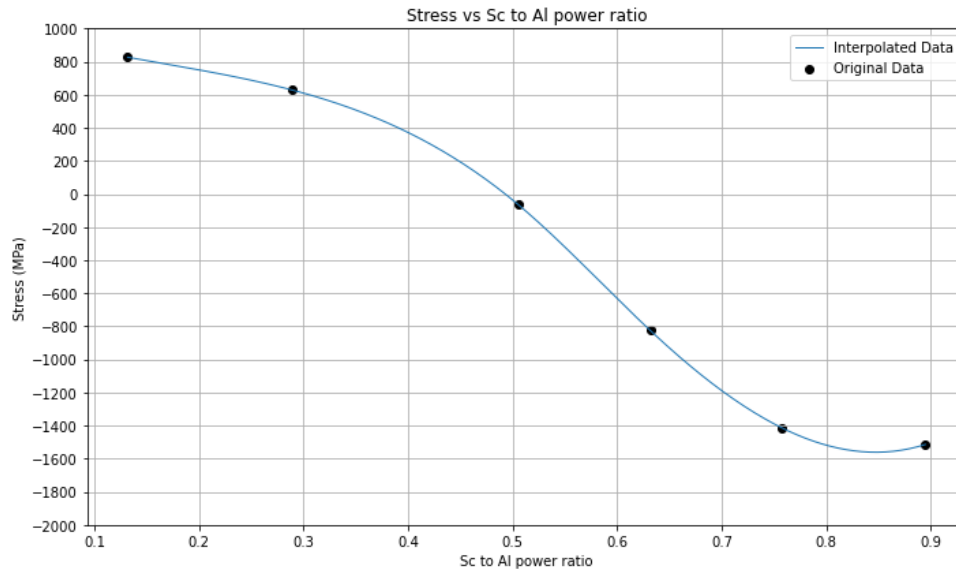


Figure 3.1 Variation of stress with the Sc to Al generator power ratio

The graph elucidates the relationship between "Sc to Al generator power ratio" and stress measured in megapascals (MPa). Observing the data closely, there is a discernible trend where an increase in "Sc%" results in a decrease in stress. Initially, at an "Sc%" of 10, the stress is at a peak of 827 MPa. However, as "Sc%" rises to 20, the stress diminishes to 628 MPa, indicating a clear reduction in tensile stress. A pivotal transition is evident between "Sc%" values of 20 and 35. Within this range, the stress not only continues its decline but also crosses the zero threshold, transitioning from tensile to compressive stress. By the time "Sc%" reaches 35, the stress has plummeted to -825 MPa. This stark shift suggests a significant alteration in the material or system's behavior or properties. As "Sc%" further escalates beyond 35, the compressive stress intensifies, albeit at a decelerating rate, hinting at a possible saturation or equilibrium state the system might be approaching. In essence, this data underscores a dynamic interplay between "Sc%" and stress, with the system exhibiting a marked transition from tensile to compressive states as "Sc%" increases.

Previously we deposited $Sc_xAl_{1-x}N$ thin films on a number Si (100) wafers to determine the ideal deposition control parameters. Based on the stress measurements obtained from the earlier mentioned samples, it is possible to gain a preliminary understanding of the relationship between N_2 dependency and film stress levels in the context of this particular sputtering process. The distance between the substrate and the target is a crucial factor in controlling the stresses. The depositions were conducted at two distinct temperatures, specifically 350 degrees and 450 degrees, in order to ascertain the optimal temperature for the film. Figure 3.2 illustrates the correlation between the level of film stress and the flow rate of nitrogen gas (N_2). At 20 mm and 30 mm of chuck height distance, the stress level is obtained for N_2 flow rate of 20 & 30 sccm at two different temperatures (350°C & 450°C). The measured data is plotted in Fig. 3.2.

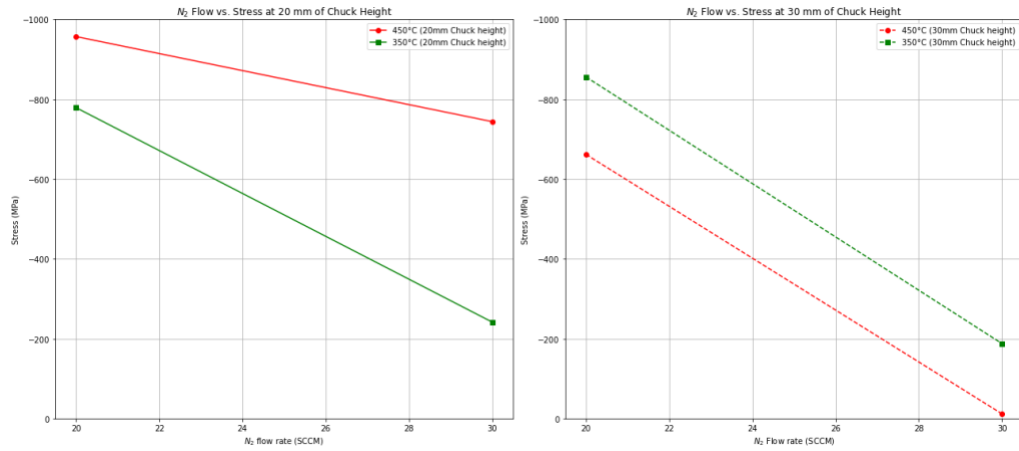


Figure 3.2 Dependence of film stress level on N₂ flow rate

The graphs presented at figure 3.2, illustrate the correlation between N₂ flow and stress at two different chuck heights, specifically 20 mm and 30 mm. At both chuck heights, the material consistently exhibits lower compressive stress at 450°C compared to 350°C, regardless of the N₂ flow rate. This observation is apparent as the red lines, which correspond to a temperature of 450°C, consistently appear higher than the green lines, which indicate a temperature of 350°C, in both subplots. Significantly, it is observed that the disparity in stress between the two temperatures becomes notably prominent when the N₂ flow rate is set at 30 standard cubic centimeters per minute (SCCM) at the 30 mm chuck height. These observations highlight the crucial influence of temperature on stress in these circumstances, where elevated temperatures result in diminished compressive stress. The uniformity of this pattern across various chuck heights underscores the predominant impact of temperature, indicating that temperature may exert a greater influence than chuck height in determining stress outcomes at the investigated N₂ flow rate. Deducing from this result we agreed to execute future depositions at 450°C and at chuck height of 30 mm.

3.2 Crystallinity of the deposited films

Crystallinity refers to the extent of regular and repetitive crystalline arrangement of atoms within a thin film layer. This characteristic significantly influences the physical, chemical, and electronic attributes of the film. A thin film exhibiting a high degree of crystallinity possesses a clearly defined lattice structure characterized by a significant extent of long-range order. These factors contribute to enhancing the overall strength, optical properties, and electrical conductivity of the film. Conversely, an amorphous or less cohesive thin film lacks a well-defined spatial arrangement, resulting in atoms being positioned differently from one another. The degree of crystallinity can be influenced by various deposition conditions, including temperature and deposition rate. The precise manipulation of crystallized thin film layers is of utmost significance in order to optimize their functionality. For our esteemed deposition condition,

measuring the crystallinity of Scandium Aluminum Nitride ($Sc_xAl_{1-x}N$) thin films is a crucial step in understanding their structural properties and optimizing their performance. Several techniques can be employed to assess the crystallinity of $Sc_xAl_{1-x}N$ films like X-ray Diffraction (XRD), Raman Spectroscopy, Transmission Electron Microscopy (TEM), Scanning Electron Microscopy (SEM), Atomic Force Microscopy (AFM) etc. Among them we used XRD to learn the crystallographic orientation and crystalline phases present in our deposited film. We also used SEM to see the grain sizes and orientation of the top surface of the film and AFM to know the details about the surface topography, roughness and grain morphology. The irregular crystal lattice orientation creates abnormal orientated grains (AOG's) in the film that can be depicted by viewing through SEM or AFM.

3.2.1 Detecting crystallographic orientation using XRD technique

X-ray diffraction (XRD) is a highly effective methodology employed for the examination of the crystallographic phases that exist within thin films [26]. The constructive approach described herein is predicated upon the interaction between X-rays and the crystal lattice of a given substance, thereby enabling the determination of its atomic configuration and crystalline makeup. For our measurement, we utilized the PANalytical X'Pert Pro MPD instrument, which was equipped with a Philips PW3040/60 X-ray generator and incorporated an X'Celerator* detector. The X-ray diffraction (XRD) system utilizes an X-ray source that emits X-rays with a well-defined wavelength. The acquisition of diffraction data involves the exposure of the surface of the samples to $Cu - K_{\alpha}$ X-ray radiation, which possesses a distinctive wavelength (λ) of 1.5418 Å [27]. X-ray radiation was produced by an anode made of copper, which was energized with a voltage of 40 kilovolts (KV) and a current of 40 milliamperes (mA) directed towards the thin film sample. The detector is responsible for measuring the angles at which the X-rays undergo diffraction. The data that is obtained as a result of the experiment is commonly referred to as a diffraction pattern. The obtained diffraction pattern is subsequently examined in order to ascertain the angles of diffraction. These angles are employed in the computation of the interatomic distance within the crystal lattice. The utilization of Bragg's law, which establishes a connection between the diffraction angle and the interatomic spacing, enables the determination of the lattice parameters of a crystal lattice. The determined lattice parameters are compared to established values for various crystallographic phases of the material. This comparative analysis aids in the identification of the distinct crystallographic phase(s) that are present within the thin film. In the context of X-pert data collection software, the Gonio scan, also known as the 2θ scan, is utilized to identify the distinct peaks corresponding to various crystallographic phases within the film. The X-ray diffraction (XRD) pattern exhibits distinct diffraction peaks that are specific to each crystallographic phase. The determination of the positions and intensities of these peaks yields valuable insights into the crystal structure and orientation of the material. Peak fitting techniques are utilized in situations where there are multiple crystallographic phases or broad peaks in order to separate the diffraction pattern and obtain specific details about each individual phase. We employed a 2θ scan technique to analyze our samples in order to identify various crystallographic phases. The

magnetron co-sputtering system was employed to introduce scandium doping into an Aluminum Nitride thin film. An Omega (ω) scan was conducted at an approximate 2θ angle of 36° , with the intention of observing the Sc (0002) peak along the c-axis to the crystal surface. Figure 3.3 illustrates the Omega scan (θ) of the films that were deposited on a Si (110) substrate.

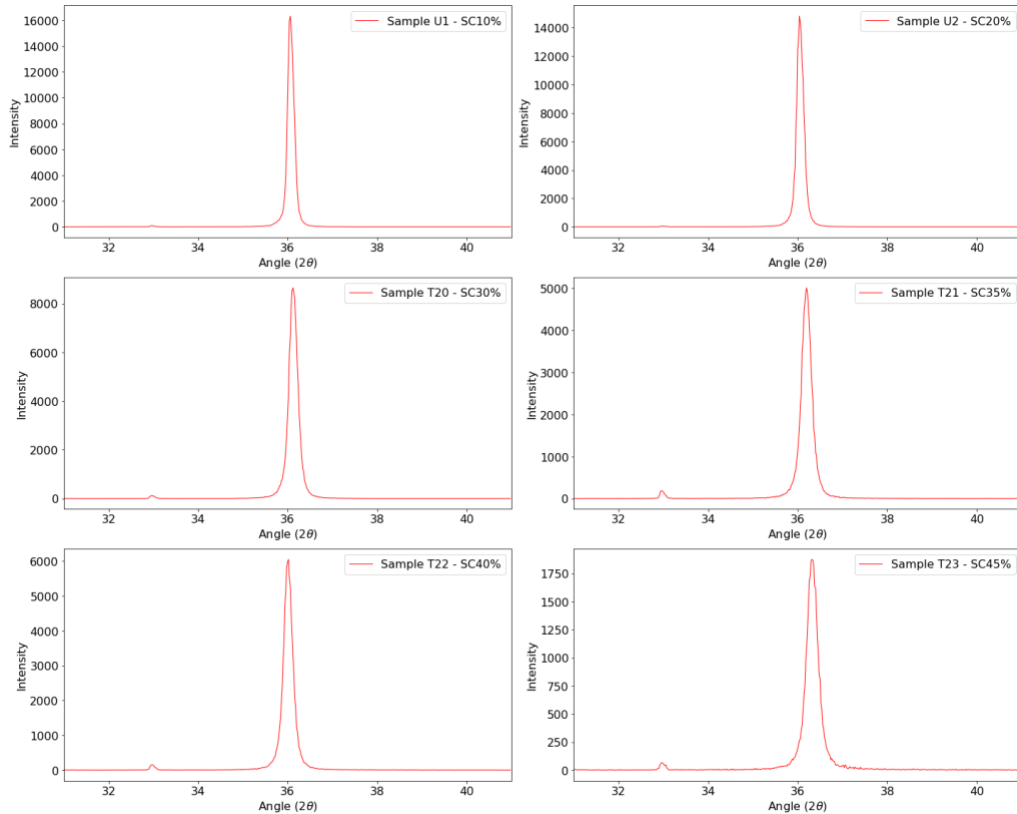


Figure 3.3 Gonio scan (2θ scan) data plotted for the films with Sc doping level of 10% - 45% deposited on Si (100)

The plots presented depict the intensity profiles of various samples containing Sc doping levels ranging from 10% to 45% as observed in X-ray diffraction (XRD) 2θ scans. The data from the XRD - 2θ scans were imported and processed using Python environment to plot these figures. The angle 2θ ranged from 31° to 41° . Each subplot in the figure represents the intensity profile of a distinct sample. Through the analysis of the highest and lowest points depicted in each graph, it is possible to make deductions regarding the degree of crystallinity or the existence of particular phases within the samples. Elevated peaks generally indicate increased crystallinity or the prevalence of a specific phase. The presence of a prominent peak at approximately 36° in the 2θ scans of all the samples indicates the strong crystal symmetry exhibited by the $Sc_xAl_{1-x}N$ (0002) phase orientation. Based on an analysis of the lattice parameters of $Sc_xAl_{1-x}N$ wurtzite crystal structure and the application of Bragg's equation of diffraction, it can be inferred that the peak observed at approximately 36°

corresponds to the $Sc_xAl_{1-x}N$ (0002) crystal phase orientation along the c-axis. A higher intensity count corresponds to a higher phase symmetry, which increases the likelihood of obtaining a well-formed crystalline structure. From the 2θ scans of these samples, it is evident that the intensity count decreases as the Sc doping level increases. It can be concluded from this result that an increase in the doping percentage of Sc leads to a decrease in the quality of the crystal structure, thereby increasing the likelihood of obtaining other crystal phases. When multiple crystal phase structures predominate in a film, the likelihood of encountering Abnormal Oriented Grains (AOGs) increases, thereby indicating poor crystal quality.

In order to determine the piezoelectric coefficient (d_{33}) of the deposited films, we conducted a deposition process for $Sc_xAl_{1-x}N$ under identical environmental conditions, but with the addition of a thin layer of Platinum (Pt). The initial step involved depositing a 200 nm layer of Pt onto a Si (100) substrate using the Evatec magnetron co-sputtering system which was needed to act as a bottom electrode while measuring the d_{33} data. Subsequently, 500 nm thick $Sc_xAl_{1-x}N$ ($x = 0.1$ to 0.45) thin layer was deposited onto the Pt layer under identical environmental conditions. In addition, the Gonio scan data for these samples was measured and visualized using the Python programming language.

Figure 3.4 illustrates the intensity counts across a consistent range of 2θ angles for $Sc_xAl_{1-x}N$ ($x = 0.1, 0.2, 0.3, 0.4$) thin layer deposited over Pt substrate. As previously observed, the peaks centered at an angle of 36° correspond to the crystal phase of $Sc_xAl_{1-x}N$ (0002) orientation along the c-axis. In addition, a noticeable peak at 40° angle can be observed, which can be attributed to the crystal phase structure of Pt (111) [28]. Based on the prominent intensity peak observed, it can be deduced that the Pt substrate predominantly exhibits a symmetrical crystal structure, accompanied by a highly favorable surface topology. It is also evident from the data that there is a consistent pattern of a decrease in peak intensity as the Sc doping level increases, suggesting a reduction in crystal symmetry along the c-axis (specifically, the 0002 orientation).

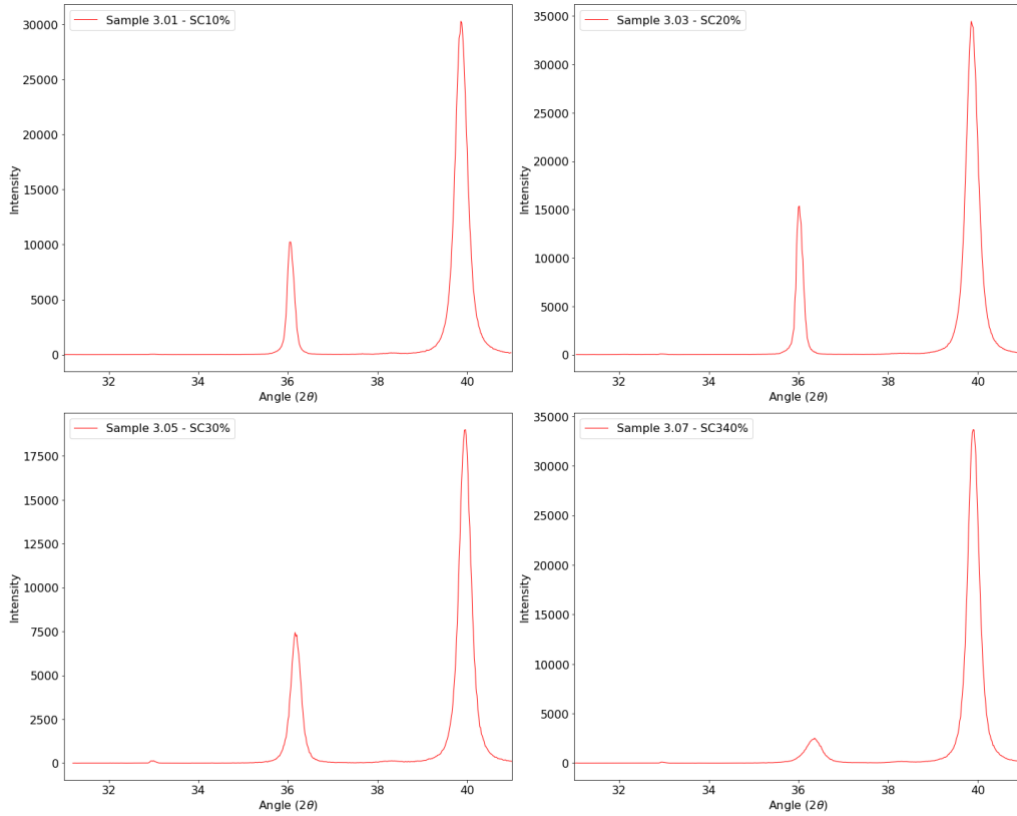


Figure 3.4 2θ scan data plotted for the films with Sc doping level of 10% – 40% deposited on Pt

3.2.2 Detecting Rocking Curve (RC) using XRD technique.

Following the confirmation of the $Sc_xAl_{1-x}N$ (0002) peak position, an Omega (ω) Scan (θ -scan) was conducted on all of the aforementioned samples. The θ scan involves stabilizing the X-Ray source handle at the $Sc_xAl_{1-x}N$ (0002) peak position and subsequently scanning a range of angles (θ) by adjusting the position of the detector. The $Sc_xAl_{1-x}N$ (0002) peak position can be accurately determined by performing a ω scan. This scan allows for the identification of the precise angles that correspond to the orientation of the lattice plane with respect to the surface of the sample. The determination of crystal structure can be inferred by measuring the Full Width Half Maximum (FWHM) of the curve that is peaked at a specific angle, based on the analysis of Omega scan data. The term commonly employed to refer to this phenomenon is known as the Rocking Curve (RC). The RC value denotes the crystallographic symmetry exhibited by a film that possesses the corresponding crystal phase. The RC (FWHM) was determined by measuring the curve at an angle of approximately 36° , which corresponds to the crystallographic orientation of the $Sc_xAl_{1-x}N$ (0002) phase. Table 3.1 represents the Rocking Curve (RC) data related to the samples we deposited.

Table 3.1 RC data for $Sc_xAl_{1-x}N$ thin films deposited on Si.

Sample ID	U1	U2	T20	T21	T22	T23
Sc doping (%)	10	20	30	35	40	45
RC	1.75	2.00	2.56	3.05	2.84	2.80

From the data extracted from the XRD scans, a figure a figure has been drawn with sub plotting the six samples RC data using Python environment.

Figure 3.5 illustrates the omega scan data pertaining to the $Sc_xAl_{1-x}N$ ($x = 0.1 - 0.45$) films that have been deposited onto a silicon (Si) substrate. We also did the

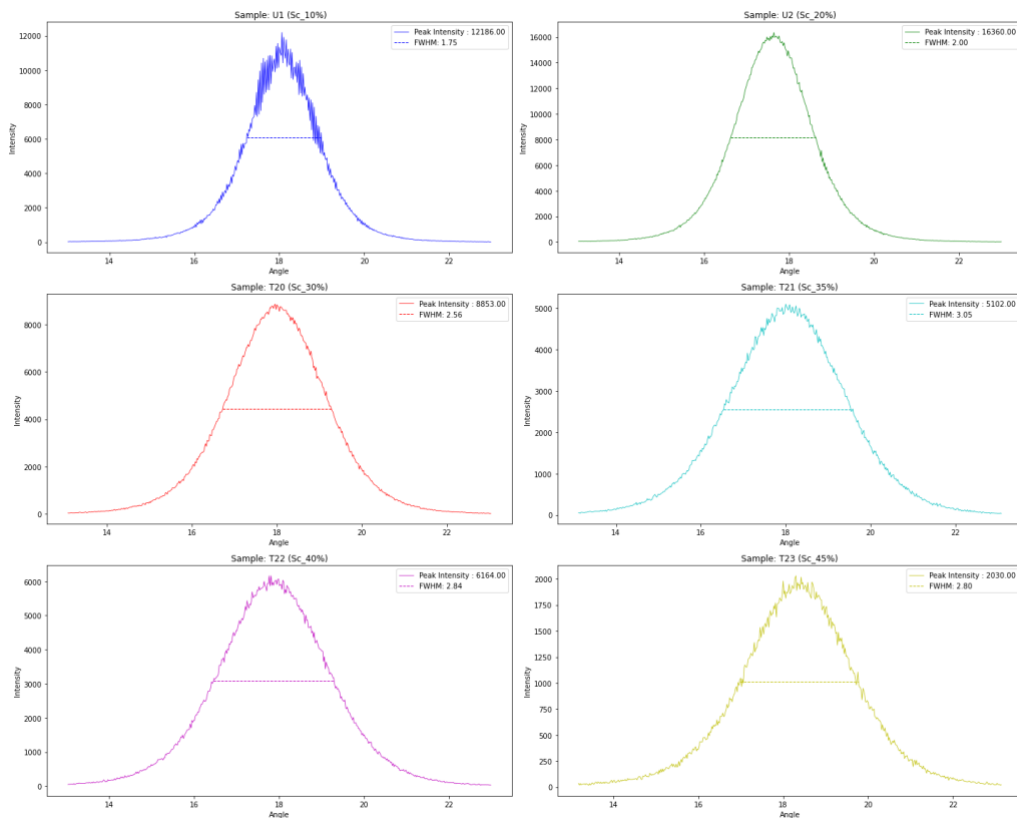


Figure 3.5 Omega Scan (ω scan) data of $Sc_xAl_{1-x}N$ ($x = 0.10, 0.20, 0.30, 0.35, 0.40, 0.45$) deposited on Si substrate with RC value

omega scan measurements on the samples deposited over *Pt* layer. Table 3.2 represents the RC data for the samples deposited on *Pt* layer.

Table 3.2 RC data for $Sc_xAl_{1-x}N$ thin films deposited on *Pt*.

Sample ID	3.01	3.03	3.05	3.07	3.09
Sc doping level	10	20	30	40	45
RC	2.28	2.02	2.19	2.31	2.96

We can see from the table that like the previous deposition on Si wafer, the trend of variation of RC value is compatible for these depositions too. Though the RC value decreased until Sc20% and then increased with Sc doping level. The data extracted from the XRD plotted in Python creating a comparison figure for the samples deposited on *Pt* layer. Fig. 3.6 portrays the representation Rocking curve data of the $Sc_xAl_{1-x}N$ samples deposited over *Pt*. It also depicts the comparison of RC data with the Sc doping level of 10%, 20%, 30%, 40% and 45%. Samples named 3.01, 3.03, 3.05, 3.07 and 3.09 represents the $Sc_xAl_{1-x}N$, where $x = 0.10, 0.20, 0.30, 0.40, 0.45$ respectively. From the fig. 3.6, It can be observed that the $Sc_xAl_{1-x}N$ film exhibits higher intensity peaks at 36 degrees with a lower percentage of Sc doping, which subsequently diminishes as the Sc doping level increases. The legend box located in the north-west corner of the graph displays various samples, each represented by a distinct color. The legend box additionally includes the full width at half maximum (FWHM) value of the RC data for each omega scan curve. It is evident that, within the Sc doping range of 10% - 20%, the RC value exhibits a decreasing trend, reaching its minimum at 2.02. Subsequently, as the Sc doping level increases, the RC value shows an upward trend, reaching 2.96 for $Sc_xAl_{1-x}N$ doped with 45% Sc. Based on the aforementioned comparisons, it can be inferred that the optimal doping percentage for the $Sc_xAl_{1-x}N$ (0002) phase orientation is 20%. Based on the composition of $Sc_{0.20}Al_{0.80}N$, it is highly probable that the (0002) plane will exhibit the predominant phase, accompanied by the most favorable crystallographic symmetry.

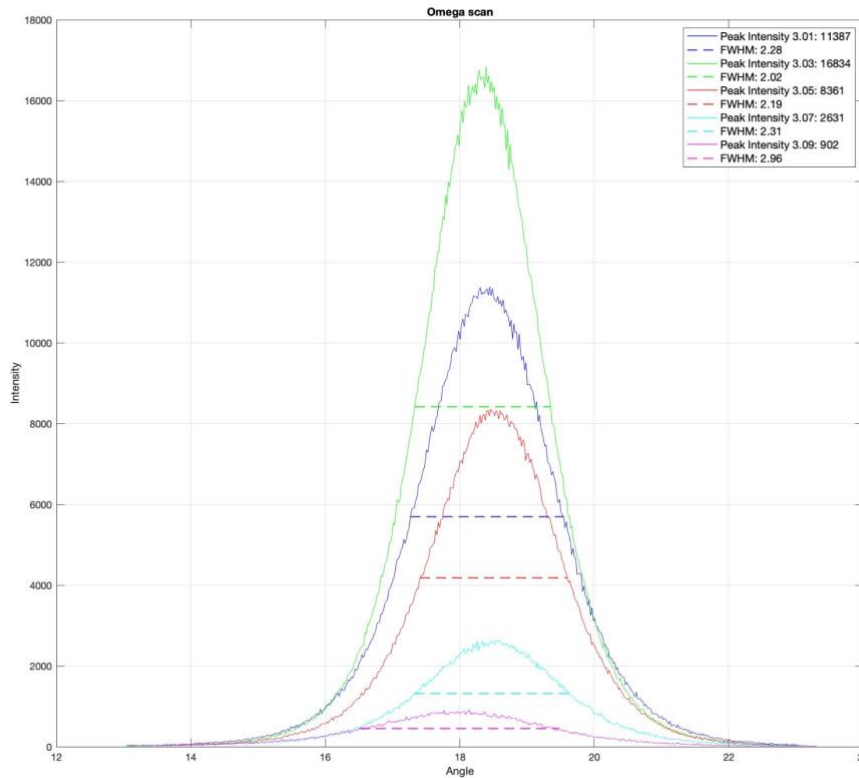


Figure 3.6 Omega Scan (ω scan) data of $Sc_xAl_{1-x}N$ ($x = 0.10, 0.20, 0.30, 0.40, 0.45$) deposited on Pt layer with RC value

3.2.3 Detecting crystal phases using XRD technique

In an attempt to comprehend the underlying cause of the decrease in peak count as the Sc% increases in the film, a comprehensive $\theta - 2\theta$ scan was conducted across the range of 20° to 80° for films with higher Sc concentrations (30%, 40% and 45%). Figure 3.7 presents a graphical depiction of the $\theta - 2\theta$ scan data, which has been plotted within the Python programming environment. The data pertains to ScAlN ($x=0.30, 0.40, 0.45$) films that have been deposited on a Pt layer. Multiple peaks were detected at various angles in films with higher concentrations of Sc, which were not observed in films with lower Sc percentages.

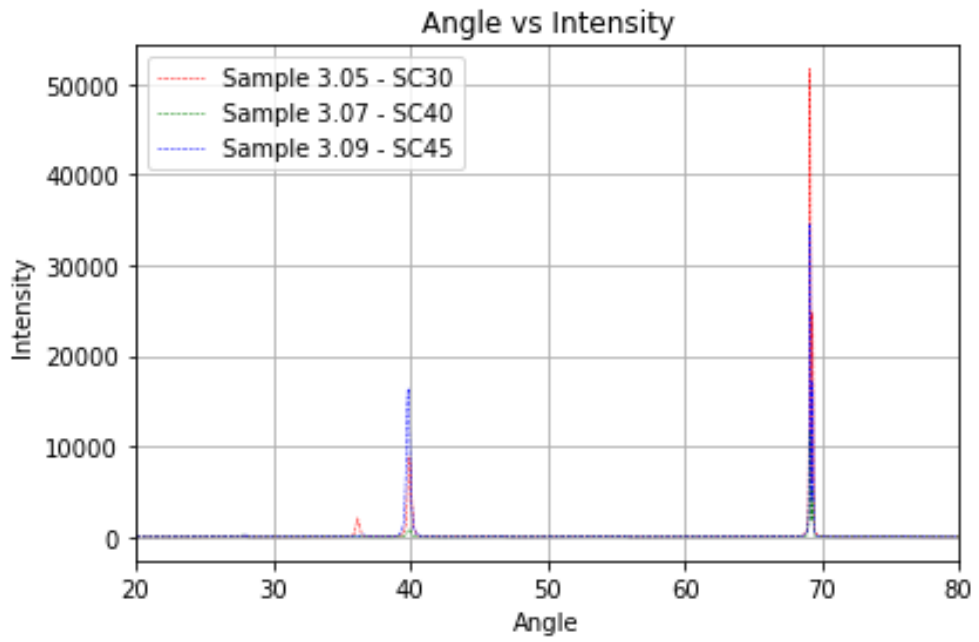


Figure 3.7 Angle vs Intensity plot from $\theta - 2\theta$ scan data deposited on Pt layer.

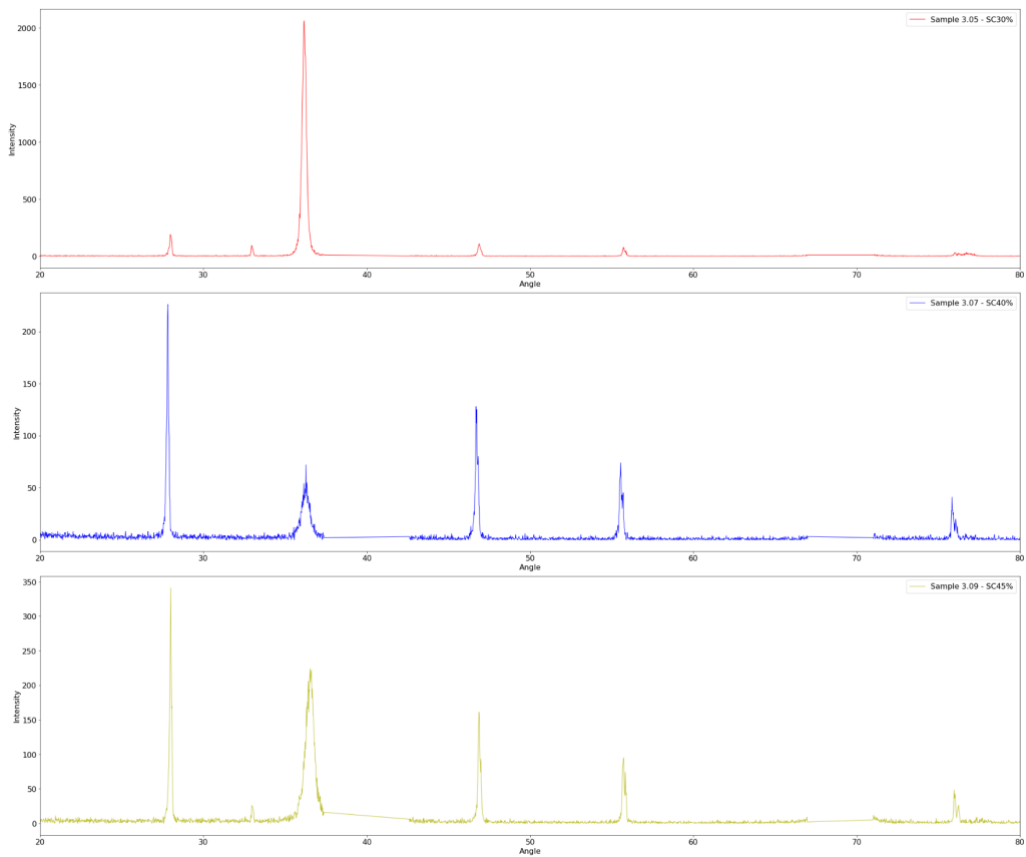


Figure 3.8 Angle vs Intensity plot from $\theta - 2\theta$ scan data deposited on Pt layer with filtered data.

From the fig. 3.7, it can be noticed that there are three peaks visible in the 2θ scan of Sc30% - Sc45% doped thin films. It has been established that the Pt (111) crystal phase exhibits an intensity peak at 40° [28], while the Si (400) crystal phase demonstrates an intensity peak at 69° [29]. In our investigation, we explored additional peaks and discovered that higher levels of Sc doping give rise to other crystal phases in ScAlN although we cannot discern those peaks in this figure. To take a closer eye of those peaks, we filtered out the data representing Pt (111) and Si (400) crystal axis and plot the graph again. Figure 3.8 represents the filtered data which shows the other peaks rather than ScAlN (0002) peak. We can see the probable crystallographic axis peaks at fig. 3.8. We are not sure which crystal orientation these peaks represent, but it is sure that increasing the Sc doping level arose those peaks. This matter needs further research to detect the other peaks from the $\theta - 2\theta$ graph of our samples. If they represent the other ScAlN crystallographic phases, that would make sense that we are losing (0002) phase orientation dominance along c-axis. This might be the reason why the crystal phase symmetry of ScAlN (0002) diminishes and the specific polarization orientation is lost at higher Sc concentration. Higher levels of Sc doping are expected to result in a deterioration of crystallographic symmetry and surface topography. In the subsequent section, we conducted an analysis of surface topography in order to validate our hypothesis.

3.3 Detection of AOG's using SEM

The identification of atypically aligned grains in materials through the utilization of a Scanning Electron Microscope (SEM) predominantly entails the examination of the material's microstructure and crystallographic characteristics. The scanning electron microscope (SEM) is an imaging instrument that utilizes electron beams rather than photons to generate visual representations. Scanning electron microscopes (SEMs) have significantly contributed to the advancement of research in the medical and physical science domains since their inception in the 1950s [30]. The scanning electron microscope (SEM) is a scientific instrument that utilizes electron beams, rather than conventional light, to generate highly magnified images. An electron gun is utilized to generate a stream of electrons at the uppermost part of the microscope. The trajectory of the electron beam within the microscope is vertically oriented and confined within a vacuum environment. The beam undergoes propagation through electromagnetic fields and is subsequently directed towards the sample via the utilization of lenses that serve to concentrate the beam. Upon interaction with the sample, the incident beam induces the emission of electrons and X-rays from the sample. Detectors are responsible for the collection of X-rays, backscattered electrons, and secondary electrons, subsequently converting them into a signal that is transmitted to a screen resembling that of a television display. The aforementioned process results in the generation of the ultimate visual representation.

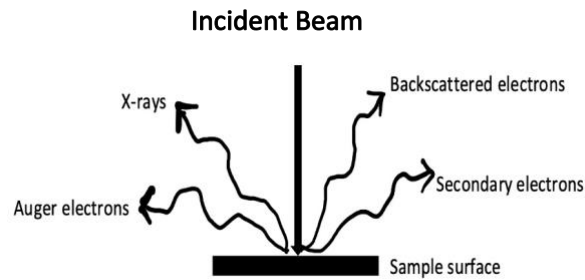


Figure 3.9 Schematic of SEM procedure

The term "abnormally oriented grains" pertains to grains present in a polycrystalline substance that exhibit orientations that deviate significantly from the prevailing crystallographic orientation. The scanning electron microscope (SEM) is employed for the acquisition of high-resolution images depicting the microstructure of the sample. In the imaging mode known as backscattered electron (BSE), variations in brightness can be observed among different crystallographic orientations. These variations arise from disparities in atomic number and crystallographic orientation. Regions exhibiting distinct brightness or contrast may be readily discerned as areas containing grains that are abnormally oriented. Scanning electron microscopy (SEM) images have the capability to offer orientation contrast by detecting variations in crystallographic orientation. Grains that are oriented in an abnormal manner may display contrasting characteristics in comparison to the grains in their vicinity. Nevertheless, it is crucial to acknowledge that relying solely on SEM may not consistently yield distinct differentiation for nuanced variations in orientation. In this study, the Zeiss Supra 25 Field Emission Scanning Electron Microscope (FE-SEM) was employed for our research purposes. The resolution of the system is on the order of 2 nanometers, while the accelerating voltage can reach a maximum of 20 kilovolts. The emitter utilized in this study is of the thermal field emission type, while the detector employed is a high-efficiency In-lens detector. The system is equipped with SmartSEM™, which is compatible with Windows® XP. It can be operated using a mouse, keyboard, and joystick, and also offers the option of using a control panel for enhanced functionality. This setup allows for efficient operation and image capture. We used mostly 5KV accelerating voltage to scan our samples. Fig. 3.10 shows the SEM scans of our samples. These samples are the $Sc_xAl_{1-x}N$ ($x = 0.1, 0.2, 0.3, 0.35, 0.40, 0.45$) thin films deposited over Si (100). We did the scan at 10 KX and 20 KX zoom factor to observe the AOG's clearly which indicates the scan size is $1 \mu m$ and $200 nm$ respectively. The $ScAlN$ thin film surface deposited on Si can be observed in Figure 3.10. Each subplot is labeled with the corresponding sample, denoted as (a) and (b), representing the pictures captured at magnification levels of 10 KX and 20 KX for each respective sample. The dimensions of the object under observation are 1 micrometer and 200 nanometers at the 10,000X and 20,000X magnification levels, respectively. The images also provide pertinent information such as the magnification level, scan length, applied accelerated voltage, working distance, and the name of the signal detector. We generally used 6 KV EHT as applying higher than this value generates a charge accumulation on the surface and visualize a dark shade in the image.

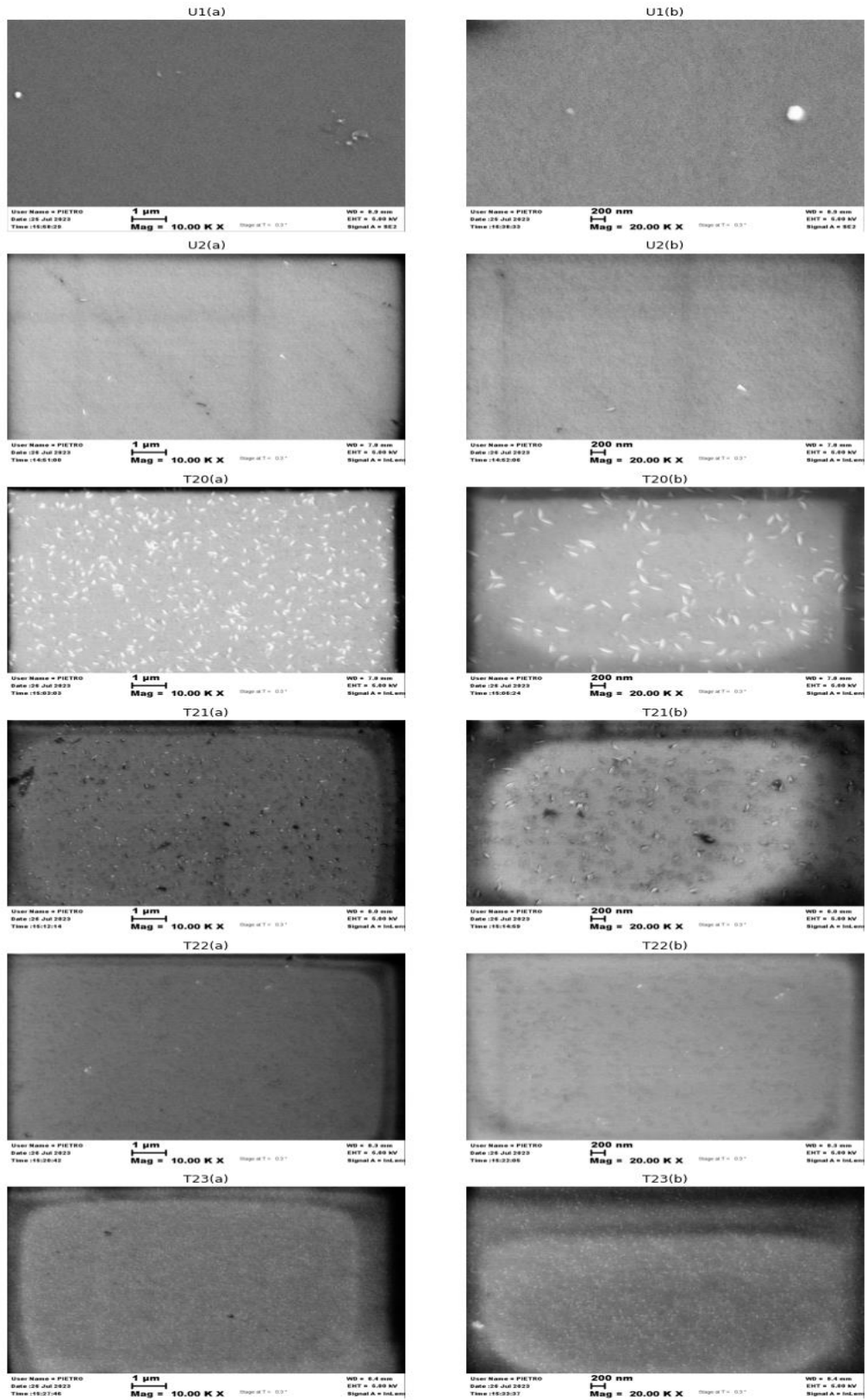


Figure 3.10 SEM images of ScAlN thin films deposited on Si

Although certain photos may exhibit areas of dark shading, these occurrences can be attributed to the accumulation of charge on the surface of the sample. Efforts were made to mitigate its presence, albeit complete eradication proved unattainable. However, the discernible traits we seek can be readily observed in the collected photos. On the film's surface, when Sc is doped with 10% and 20%, there are actually a few abnormally oriented grains (AOGs), as can be seen in the images. AOGs are more prominent and easily visible on the surface of the 30% Sc doped film. The film surface level is quite rough with 35% Sc doping, although the AOG percentage is likewise high. Thus, the number of AOGs is increasing as we increase the percentage of Sc doping in our film. As a result, the film has surface grains with various orientations. However, we scarcely see any AOGs that are evident at our magnification level for 40% and 45% Sc doped ScAlN films. We can observe several contrast deviations in the shape of AOGs at a magnification level of 20 KX, although we are unsure if these are AOGs or if they are the result of a rough surface texture. We must further reduce the scan area with clear vision of the microscope in order to make the surface plainly visible. We require a more potent electron scanning microscope with modern technology because those shapes are extremely small and cannot be observed at 200 nm scanning length. Whether the shapes are AOGs or not is still up in the air at this time. If they are AOGs, they are substantially smaller than the AOGs seen in previous films with lesser levels of Sc doping, if they are AOGs. If they are not AOGs, they may develop as a result of an uneven surface texture. Therefore, additional research is required to confirm these hypotheses and determine the true surface topography of the formed films with increasing Sc doping levels. Additionally, an examination was conducted on the remaining samples that were deposited above the Pt layer. Fig. 3.11 shows the images of SEM investigation of the ScAlN thin films that were deposited on Pt layer. Given that the concentration of Sc doping and the thickness of a sample are equal, it is expected that samples with equivalent Sc doping levels would exhibit very similar surface characteristics. Fortunately, the deposition of these films atop a Pt layer yielded improved surface pictures during SEM analysis. The films with increased Sc% doping exhibit partial confirmation of the presence of Abnormally Orientated Grains. Furthermore, the occurrence of dark hues resulting from charge accumulation was effectively mitigated. The films exhibit the presence of AOGs, which strongly suggest a comprehensive understanding of the preceding films. In films with lower concentrations of Sc doping, a reduced proportion of AOGs was observed, whereas films with higher Sc doping concentrations exhibited a higher proportion of AOGs. Although the majority of Sc-doped films exhibit AOGs that are significantly lower in size. It is anticipated that films with increased Sc% will exhibit more unfavorable surface properties. In order to acquire more comprehensive information, we conducted an investigation of the surface topography and roughness level of the deposited films using Atomic Force Microscopy (AFM). The subsequent section presents the Atomic Force Microscopy (AFM) research, including accompanying photos and quantified roughness measurements of the films under examination.

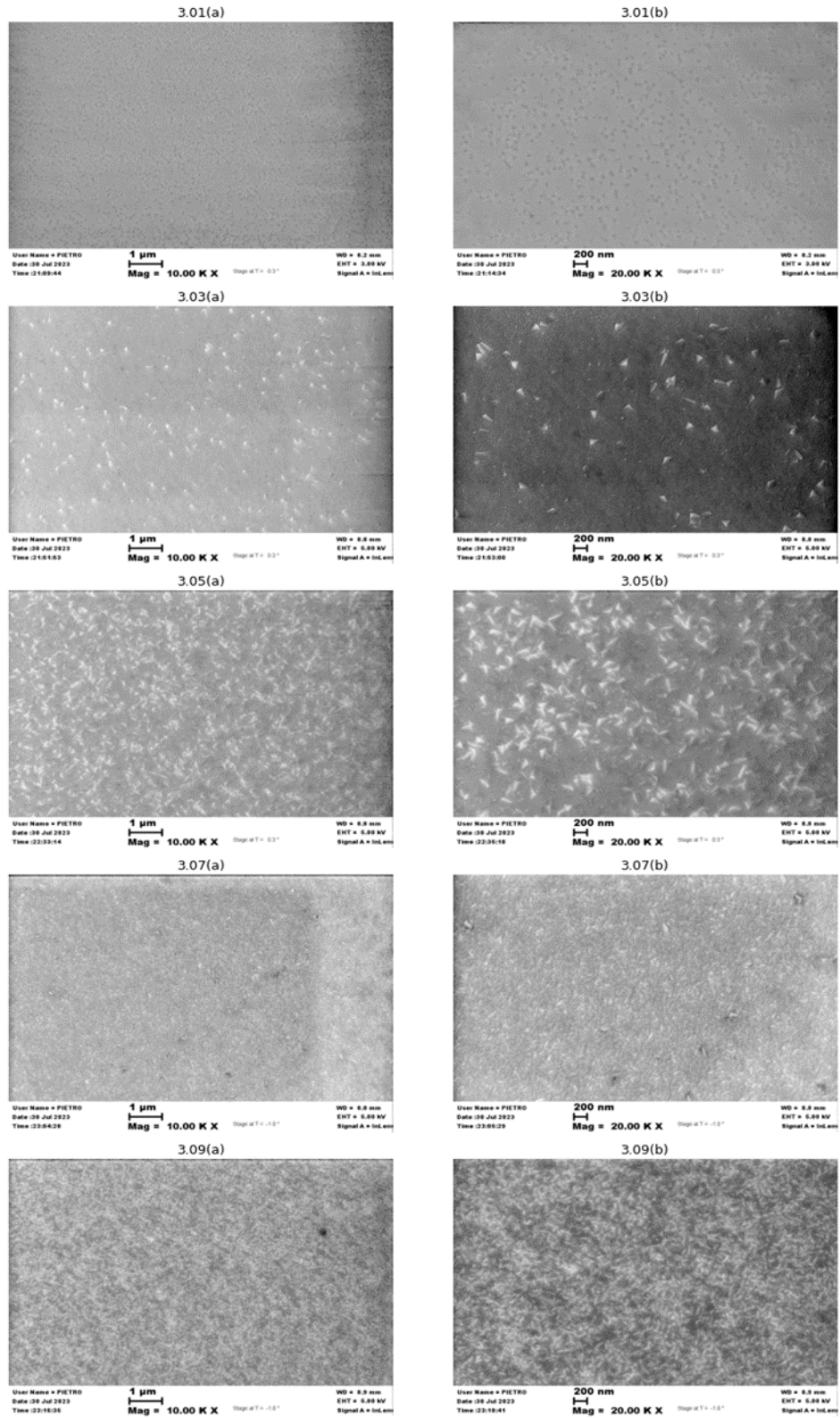


Figure 3.11 SEM images of *ScAlN* thin films deposited on *Pt* layer.

3.4 Surface topography with AFM

3.4.1 Surface imaging

Atomic force microscopy (AFM) is a technique employed for the examination of materials at the nanoscale, offering high-resolution imaging capabilities. The operational principle involves the translation of a finely pointed tip along the surface of a specimen, while simultaneously monitoring and analyzing the dynamic interactions between the tip and the sample surface. Atomic Force Microscopy (AFM) provides valuable insights into various aspects of a surface, including its topography, mechanical characteristics, and certain chemical reactions. AFM has a better resolution than SEM and can approach genuine atomic resolution, which is comparable to scanning tunneling microscopy and TEM [31]. Atomic force microscopy (AFM) employs a diminutive cantilever that is affixed with a pointed tip at its unrestrained extremity. The tip engages in interaction with the surface of the sample. When the tip is brought into proximity with the sample surface, a multitude of forces are engaged. The forces at play encompass van der Waals forces, electrostatic forces, magnetic forces, and repulsive forces that arise when the tip approaches the surface in close proximity. The Atomic Force Microscopy (AFM) system effectively regulates a consistent interaction force between the tip and the sample by modulating the vertical position.

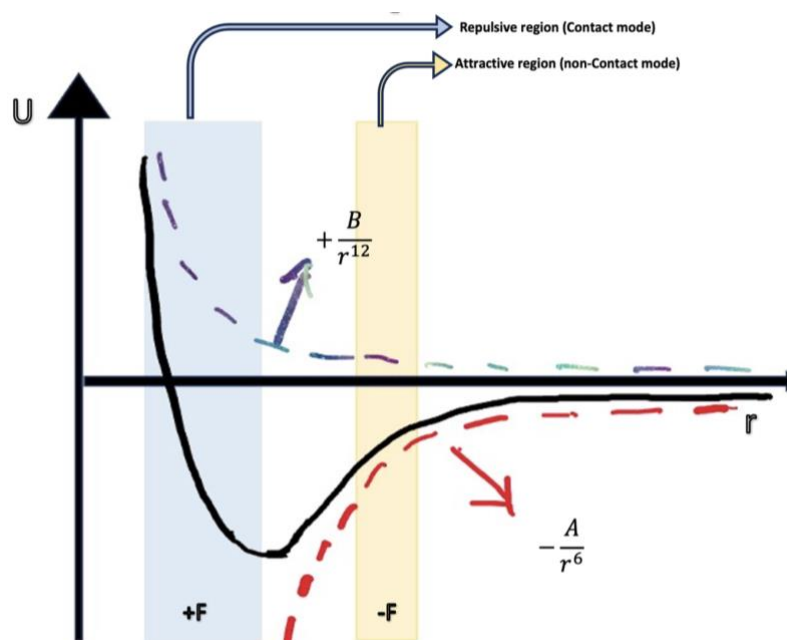


Figure 3.12 Interatomic interaction forces acting in AFM process.

In the scanning procedure, a laser beam is directed towards the posterior region of the tip, which has been coated with a reflecting substance. The laser beam undergoes reflection upon encountering a highly reflective surface, subsequently impinging upon a photodetector screen. The cantilever is systematically moved across the surface of the sample in a raster pattern. The cantilever's vertical displacement is continually

modulated in order to sustain a consistent contact force, thereby generating a topographic representation of the surface of the sample. When the tip of the instrument comes into contact with irregularities or indentations on the surface of the sample, it undergoes a deflection from its initial position, resulting in a corresponding movement of the laser beam. The detection of this movement is accomplished through the utilization of a photodetector, which subsequently transmits the observed signal to a circuit with a high gain amplifier [32].

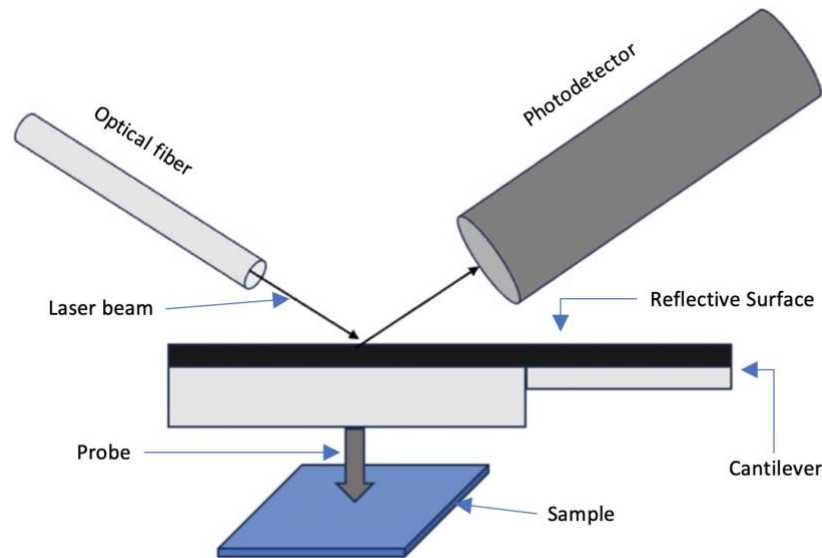


Figure 3.13 Schematic diagram of AFM scanning procedure

For our experiment we used Park XE-7 Atomic Force Microscope (AFM) made by Park Systems, a leading AFM manufacturer. The Park XE-7 is a research-grade atomic force microscope (AFM) that offers a cost-effective solution [33]. It is equipped with the Non-Contact Mode™, which ensures a longer lifespan for the tip and reduces the potential danger of injuring the sample. The system comprises of a high-force flexure Z-scanner that is guided and has a scan range of 25 micrometers. Additionally, it incorporates a single module flexure XY-scanner that is equipped with closed-loop control. The Smart-Scan software is specifically designed for the purpose of system control and data collecting, while XEI serves as the software dedicated to data analysis. The device incorporates many operation modes, although we specifically employed the non-contact mode to conduct surface scanning of our samples. Figure 3.14 presents the surface imaging of the *ScAlN* thin films that have been deposited on a silicon substrate. Each subplot is labeled with its corresponding sample numbers. The scan area was $5 \times 5 \mu\text{m}^2$.

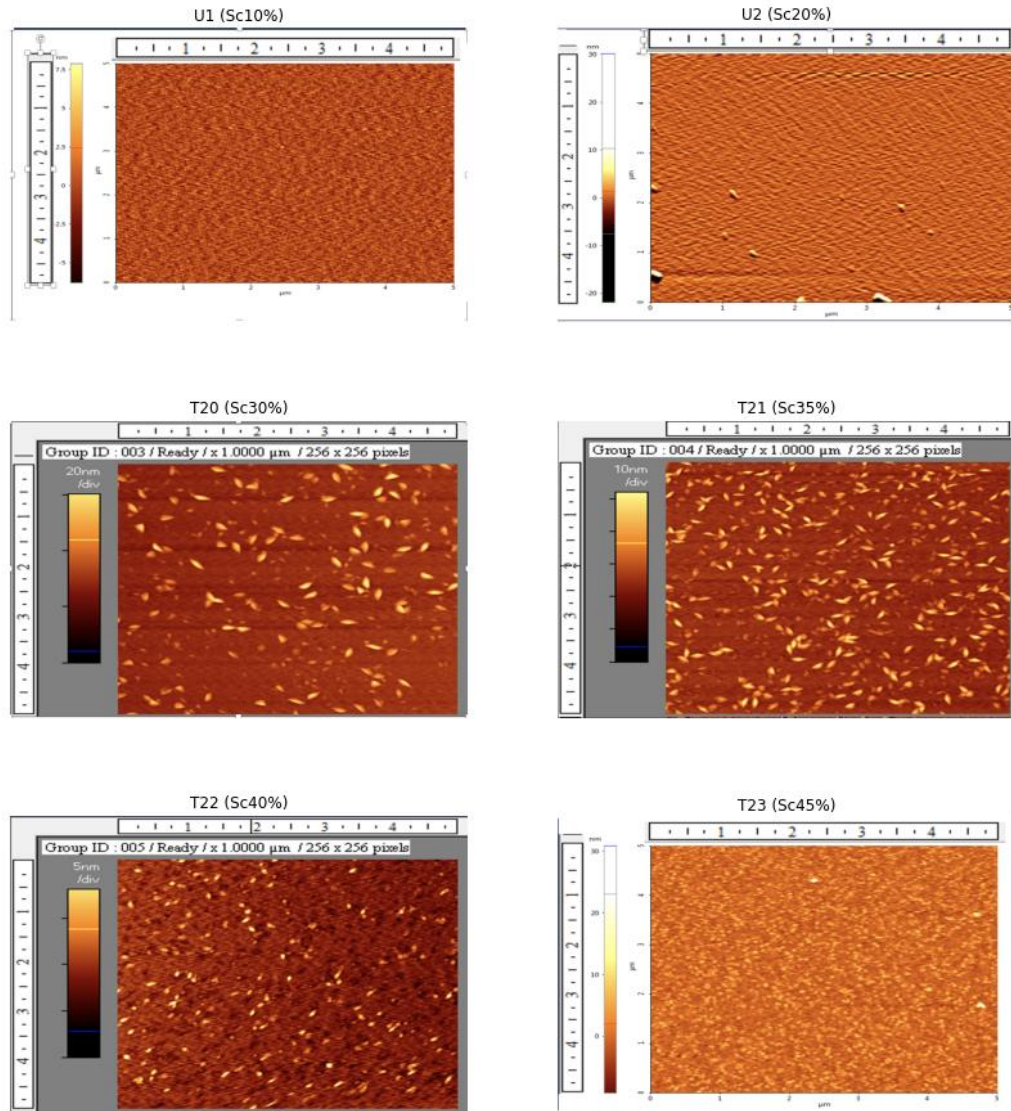


Figure 3.14 AFM scan images of the $ScAlN$ films deposited on Si

Based on the data presented in Figure 3.14, it is evident that $ScAlN$ thin films doped with Sc10% and Sc20% exhibit a limited number of Abnormal Oriented Grains (AOG's) on their surfaces. In contrast, an increase in the doping level to 30% and 35% is shown to result in a significant presence of AOG's on the surface of the films. The number of AOG's appears to be increasing in correlation with the observed increase in Sc doping levels. In the case of a 40% Sc doped film, it is seen that there is a reduced presence of AOG's, whereas a significant number of unidentified, black-shaped grains are present. Moreover, while examining a surface doped with 45% Scandium, it becomes apparent that the grains present are of significantly smaller size and possess a rough surface texture. The identification of those entities as AOG's cannot be definitively confirmed. The scanning electron microscopy (SEM) images of these films revealed similar rough

surface, however, it is not possible to confirm the presence of AOG's due to significant differences in grain size and texture compared to previously confirmed films. In order to validate the authenticity of these grains, it may be necessary to do further scanning at a smaller scale, specifically within the nanometer range. However, the atomic force microscopy (AFM) images provided us with enhanced visual representations of the surface characteristics of our materials. Furthermore, an examination was conducted on the surface properties of the *ScAlN* thin films that were placed onto a Pt layer. Given that the Sc doping level remains constant throughout the relevant samples, it is anticipated that a comparable surface topography will be seen for these samples.

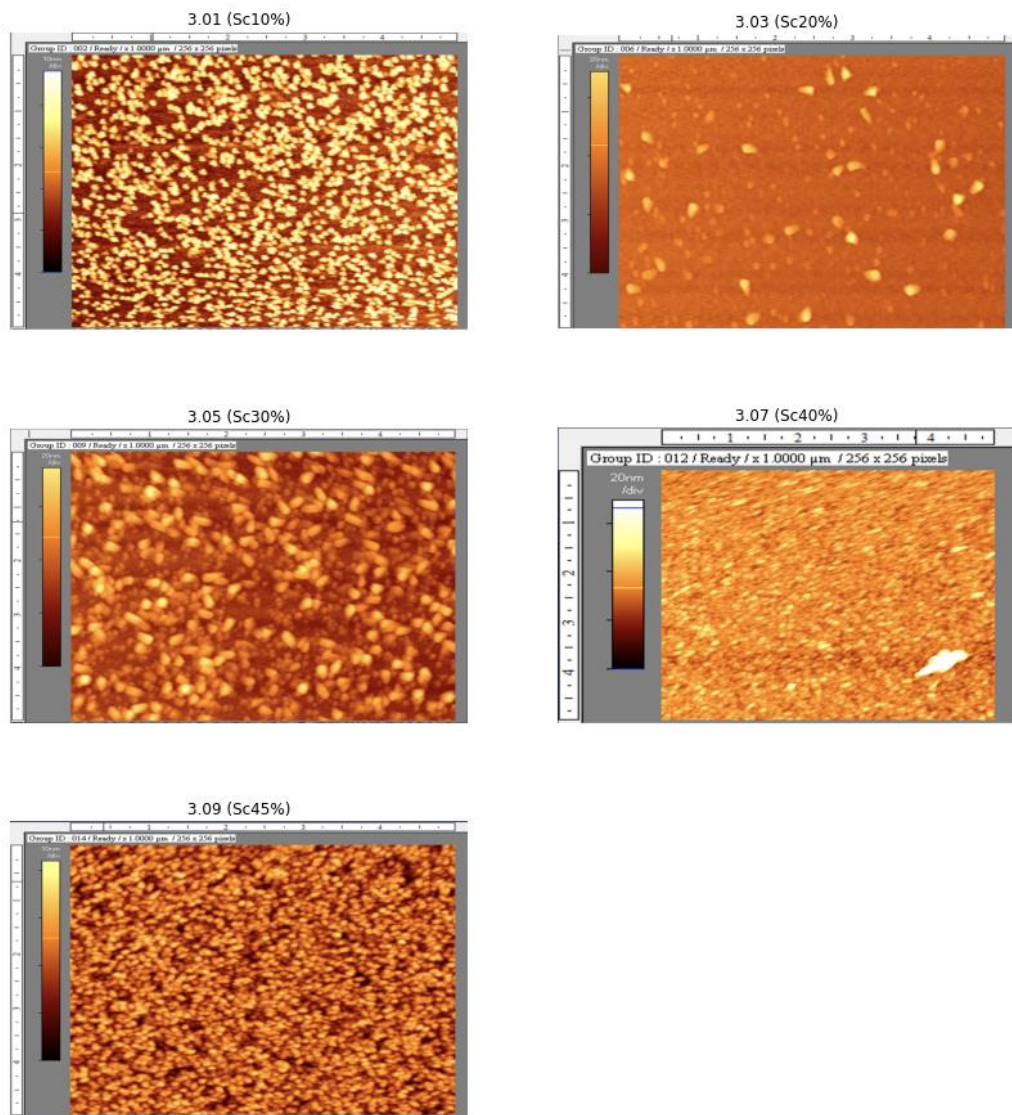


Figure 3.15 AFM scan images of the *ScAlN* films deposited on Pt

Despite the fact that the 10% Sc doped *ScAlN* thin film deposited over *Si* did not exhibit any AOGs, the film deposited on *Pt* had a lot of tiny grains visible on its surface. In this scenario, it is not possible to definitively ascertain whether the object in question belongs to AOG or not. It is postulated that the aforementioned grains are not of AOG origin, as evidenced by their comparatively small size and distinctive morphologies. The rough surface texture of the deposited layer is quite significant. In order to get a higher level of specificity in detection, it may be necessary to employ more sophisticated scanning technologies such as Transmission Electron Microscopy (TEM). The surface of the Sc-doped film, with doping concentrations of 20% and 30%, exhibited a similar AOG pattern to that observed in prior films deposited on silicon substrates. The films doped with 40% and 45% Sc exhibit a significantly rough surface characterized by numerous tiny grains of varying shapes. However, it is not possible to definitively determine the presence of AOGs in this context. Further study is required to ascertain the specific properties and surface topography of these grains.

3.4.2 Surface roughness detection

Following the acquisition of surface topography images of our samples, we proceeded with exporting the scan to XEI Image processing software, which is integrated with the AFM equipment developed by Park Systems. The software was utilized to correct the tilt observed in the scan images by removing the slope. Afterwards the execution of the tilt correction, we proceeded to quantify the surface roughness. The arithmetic mean (R_a) was calculated using the height parameters of the entire image. Table 3.3 presents the data pertaining to the surface roughness (R_a) of the samples under consideration.

Table 3.3 Surface roughness data for experimental samples

Sample Label	Sc%	Roughness (R_a) in <i>nm</i>	Deposited on
U1	10	0.922	<i>Si</i>
U2	20	0.899	
T20	30	2.578	
T21	35	2.995	
T22	40	1.038	
T23	45	1.718	
3.01	10	7.917	<i>Pt</i>
3.03	20	2.352	
3.05	30	8.033	
3.07	40	3.740	
3.09	45	2.058	

From roughness data table 3.3, we plotted the roughness variation with respect to Sc to Al power ratio in our samples. Figure 3.16 represents the roughness variation with Sc doping level for both films deposited on Si and Pt.

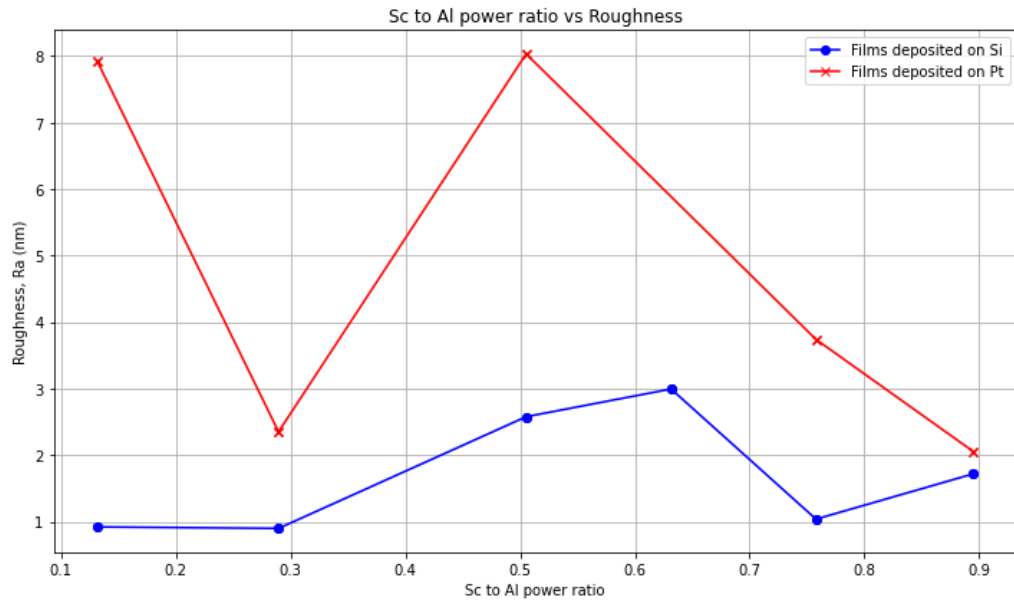


Figure 3.16 Variation of surface roughness with Sc to Al generator power ratio

As Sc to Al power ratio is correlated with the Sc doping level, we can substitute Sc to Al power ratio by Sc%. We can see the roughness variation of the film we deposited over Si and Pt layers. The red points indicate the roughness values of the film surfaces that were deposited on Pt layer and the blue points indicate the roughness values of films surfaces deposited over Si. It is noticeable that the average roughness level is higher for the films that were deposited on Pt. We needed Pt layer to act as a bottom electrode connection to measure the piezoelectric coefficient of the films. Nevertheless, depositing same film over Pt electrode made the surface worse than we anticipated. However, for 20% Sc doping in the *ScAlN* thin film made the surface less rough compared to the other doping levels. After determining the surface roughness characterization, we proceeded to extract the piezoelectric coefficient (d_{33}) of the films we deposited.

Chapter 4: Piezoelectricity of the *ScAlN* thin films

4.1 Ferroelectric behavior of *ScAlN*

The first chapter of this work provided an overview of the fundamental principles underlying piezoelectricity and ferroelectricity. This chapter focuses on the ferroelectric properties exhibited by *ScAlN* thin films. The addition of scandium (*Sc*) as a dopant in aluminum nitride (*AlN*) has been shown to greatly increase the piezoelectric coefficients, as evidenced by the research conducted by Umeda et al. [34]. In this chapter, the determination of the piezoelectric coefficients of *ScAlN* films with different *Sc* doping percentages was conducted. The first chapter introduced two main categories of piezoelectric materials. The initial class demonstrates the phenomenon of pyroelectricity, whereas the subsequent class manifests the property of ferroelectricity. While it is true that not all ferroelectric materials demonstrate piezoelectric activity, it is universally acknowledged that all ferroelectric materials possess this property. Recent studies have demonstrated that films of aluminum nitride (*AlN*) doped with scandium (*Sc*) display characteristics of ferroelectricity. The crystal structure of *AlN*, as well as other *III – V* nitrides such as *InN* and *GaN*, exhibits spontaneous polarization along the *c*-axis, resulting in their classification as wurzite-type crystals. The presence of two polarization orientations, namely the N-polar and the metal-polar, within the material, which are anti-parallel to each other, is indicated by this attribute that is associated with its piezoelectricity. The *III – V* nitrides exhibit pyroelectricity but do not possess ferroelectricity due to the fact that electric forces below their dielectric breakdown threshold, when they transition from insulators to conductors, are inadequate to induce a polarization reversal. Nevertheless, the electric field necessary for inducing polarization switching in pure *AlN* films can be decreased through the process of doping with *Sc*, leading to the manifestation of ferroelectric properties. The observed polarization transition can be attributed mostly to the progressive transformation from the wurzite crystal structure of aluminum nitride (*AlN*) to the layered-hexagonal structure, similar to that of scandium nitride (*ScN*), as the level of scandium doping increases. Akiyama et al., have provided evidence that the piezoelectric behavior of solid mixtures composed of *AlN* and *ScN* exhibits a consistent increase as the *Sc* content rises, as long as the wurzite crystal structure remains intact [35]. The experimental demonstration of *ScAlN* ferroelectric hysteresis curves was initially conducted by Fitchner et al. [12]. The outcomes, in conjunction with the polarization versus electric field curve for lead-zirconate-titanate (PZT 52/48), a widely utilized ferroelectric substance, are depicted as well as with various *Sc* concentrations in Figure 3.1. The piezoelectric linearity is demonstrated to be excellent for electric fields that are lower than the coercive fields. Figure 3.1 also presents hysteresis curves for *ScAlN* films with *Sc* concentrations equal to or exceeding 27%. As previously demonstrated, the manifestation of ferroelectric properties in the nitride is dependent upon *Sc* concentrations surpassing 22%. This is due to the observed reduction in coercive fields of the material films as the level of *Sc*-doping increases. Prior to that juncture, the *Ec* values remain higher above the threshold for dielectric breakdown. When the material undergoes a transition to a ferroelectric state, its coercive field (*Ec*) and residual polarization (*Pr*) exhibit relatively high values in

comparison to commonly employed ferroelectric materials such as PZT. It is evident that as the Sc-percentile content increases, there is a corresponding decrease in the E_c and P_r values. The relationship between the Sc-percentile content and E_c values is linear, whereas the relationship between the Sc-percentile content and P_r values is non-linear.

4.2 Piezoelectric coefficients of $ScAlN$

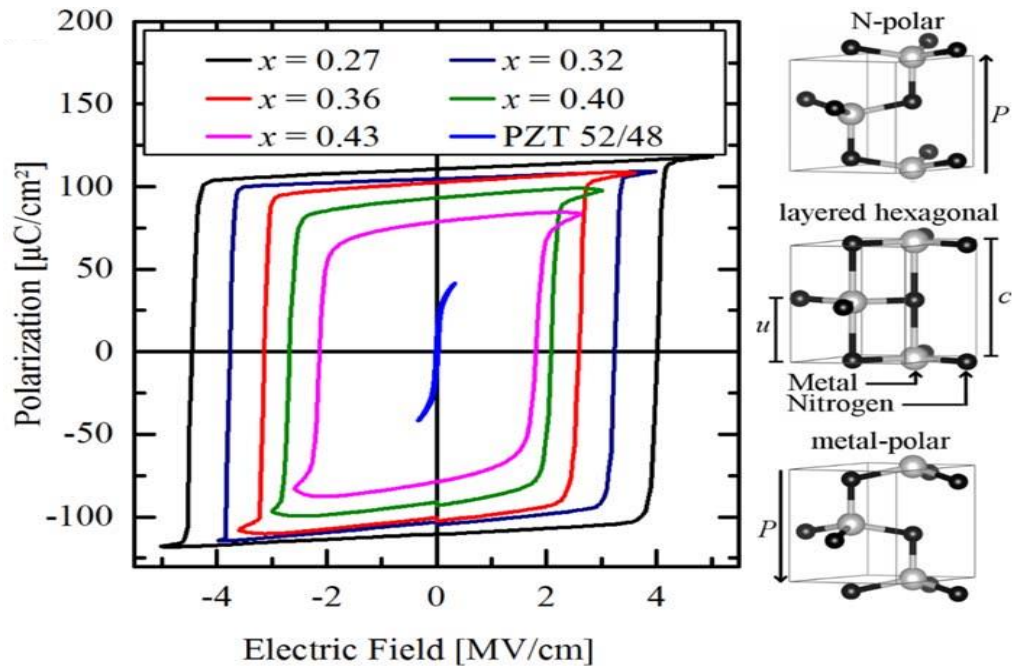


Figure 4.1 The polarization-electric field (P-E) hysteresis loops of ferroelectric $Al_{1-x}Sc_xN$ with Sc concentrations ranging from $x = 0.27$ to $x = 0.43$, as well as the P-E loop of PZT 52/48, were examined. The structures associated with the distinct polarization states are depicted on the right [12].

As previously stated in the introductory chapter, piezoelectricity refers to the capacity of specific materials to produce an electrical charge when subjected to mechanical stress, or alternatively, to undergo deformation when an electric field is applied. The compound $ScAlN$ has received significant attention owing to its potential for piezoelectric applications at high temperatures, a capability that is beyond the reach of conventional piezoelectric materials such as lead zirconate titanate (PZT). The piezoelectric coefficients, electromechanical coupling factors, and other material properties of the system can exhibit variations based on factors such as the growth process, crystal orientation, and doping. The piezoelectric characteristics of $ScAlN$ are subject to influence from various parameters, including crystal structure, composition, and the orientation of applied stress or electric field. To extract the piezoelectric

coefficient (d_{33}) of the deposited films, first we prepared the same through several process.

4.2.1 Sample preparation

As indicated in the second chapter, all samples were deposited utilizing the Magnetron Co-sputtering technology known as Evatec-CLUSTERLINE. A platinum layer with a thickness of 200 nm was placed onto a silicon substrate. In order to accurately measure the d_{33} parameter using the aixACCT DBLI system, it is necessary to subject the Si wafer to a double polishing process. The deposition of this layer was carried out for the purpose of utilizing it as a bottom electrode. A $Sc_xAl_{1-x}N$ thin film with a thickness of 500 nm was formed onto a Pt layer, where x ranges from 0.1 to 0.45. Various levels of Sc doping were implemented in order to investigate the impact of Sc doping on the piezoelectric characteristics of the film. Following the deposition of the piezo layer, it was necessary to introduce a top electrode in order to facilitate the measurement of the d_{33} parameter. Therefore, as a preliminary step, lithography was initially conducted. In the initial stage, the layer was coated with the photoresist PR-S1813 by a spinning process. Following a rigorous baking process at a temperature of 115°C, the samples were subjected to ultraviolet (UV) light exposure using a predetermined mask in the EVG-610 mask aligner. The lithographic masks utilized for patterning the structures were created using the Python package GDSPy and subsequently optimized using the K-layout software. Figure 4.2 displays the GDS file representing the intended chip. In order to fabricate the structures, the created on the top of the piezo layer referred to as the TOP mask, was employed to create the top electrode of the capacitors. The second mask, known as the VIAs mask, was utilized to establish the necessary electrical connections to the platinum (Pt) bottom electrode. It is worth noting that the Pt bottom electrode was intentionally left to cover the whole wafer during the fabrication process. It is evident that many forms with distinct geometries have been positioned on the wafer. The samples were developed using a micro-posit developer. Gold (Au) was selected as the top electrode, and the structures were fabricated utilizing the lift-off technique subsequent to the deposition of Au. The VIAs have been made through the process of selectively removing a smaller section of the piezo surface by scratching. The top and bottom electrodes that sandwich the piezo layer act as a capacitor. The chip is thereafter moved to the aixACCT DBLI system from the clean room with caution in order to accurately measure the piezoelectric coefficient. Figure 4.3 depicts an image of the completed chips patterned on the film.

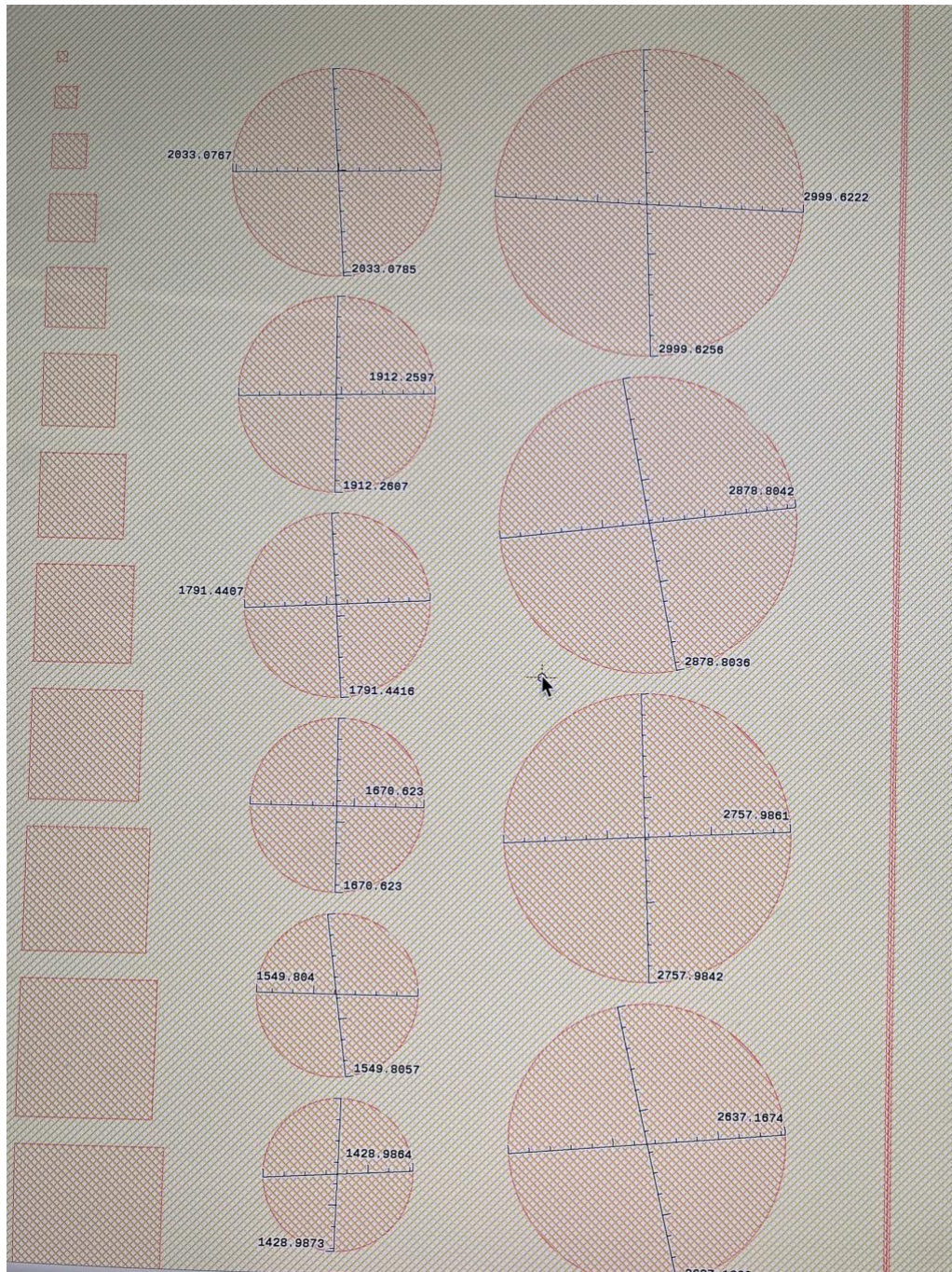


Figure 4.2 The lithographic mask created in K-Layout environment represents the top electrode shapes.

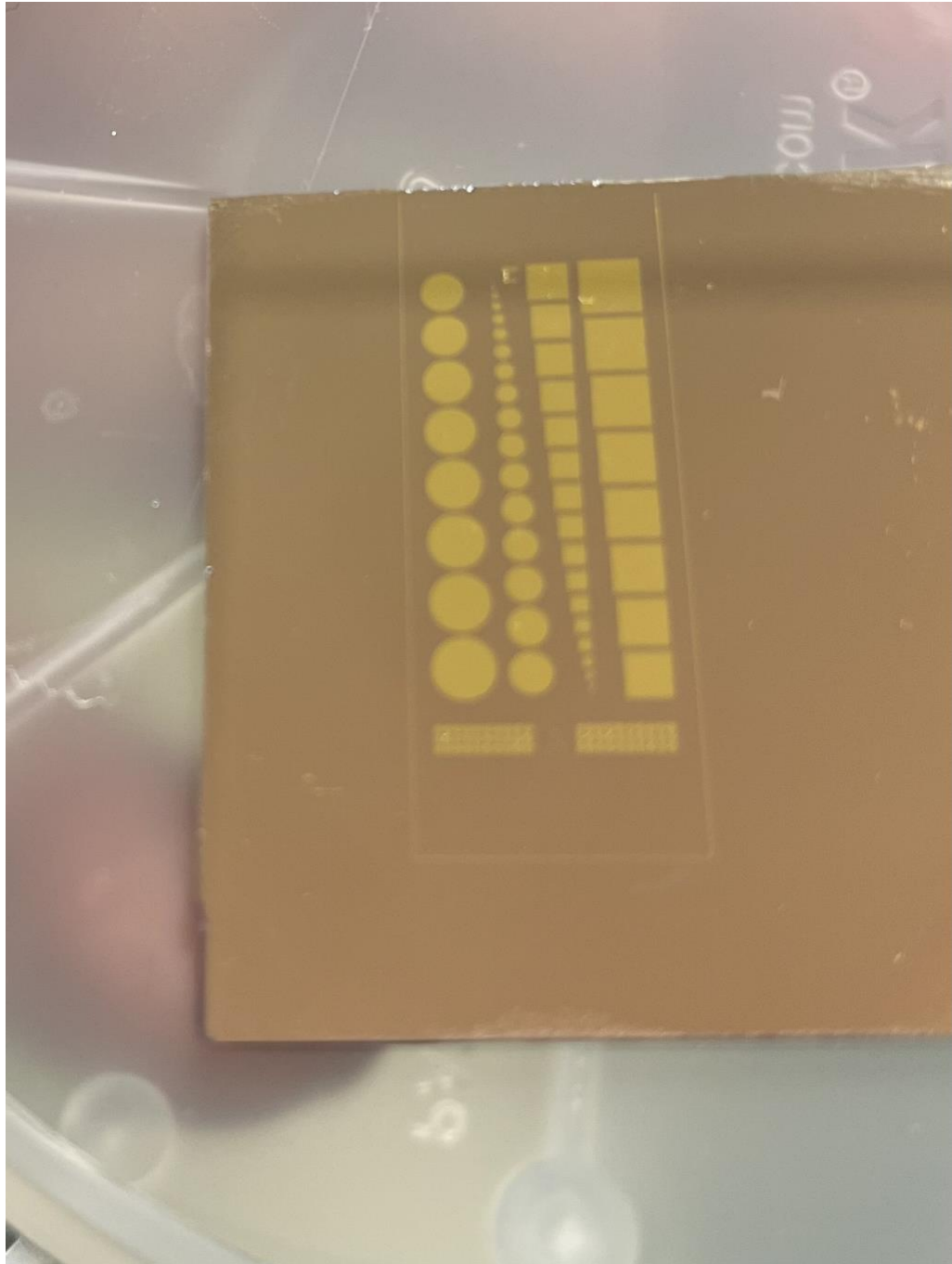


Figure 4.3 The final chip look showing the top electrode pattern with Gold (Au).

4.2.2 aixACCT DBLI

The aixACCT DBLI tool is designed for the characterization of thin films with electric, piezoelectric, and ferroelectric properties. The acronym DBLI refers to Double-Beam Laser Interferometer, a device utilized for the purpose of conducting piezoelectric characterization and extracting piezoelectric coefficients. The tool comprises a computer equipped with the AixPlorer and aixACCT DBLI Assistant software applications, facilitating the execution of measurements using a Graphic User Interface (GUI). In addition, the system includes a high-voltage amplifier with the capacity to provide an input voltage of up to 400 V and a current of 100 mA, as well as a vibration suppression mechanism. The DBLI module encompasses an optical setup and a chuck that facilitates the placement and characterization of wafers or individual chips. The pads on the chip are subjected to probing using sharp points made of tungsten. According to the DBLI user manual, the optical component arrangement is given in Fig. 4.4.

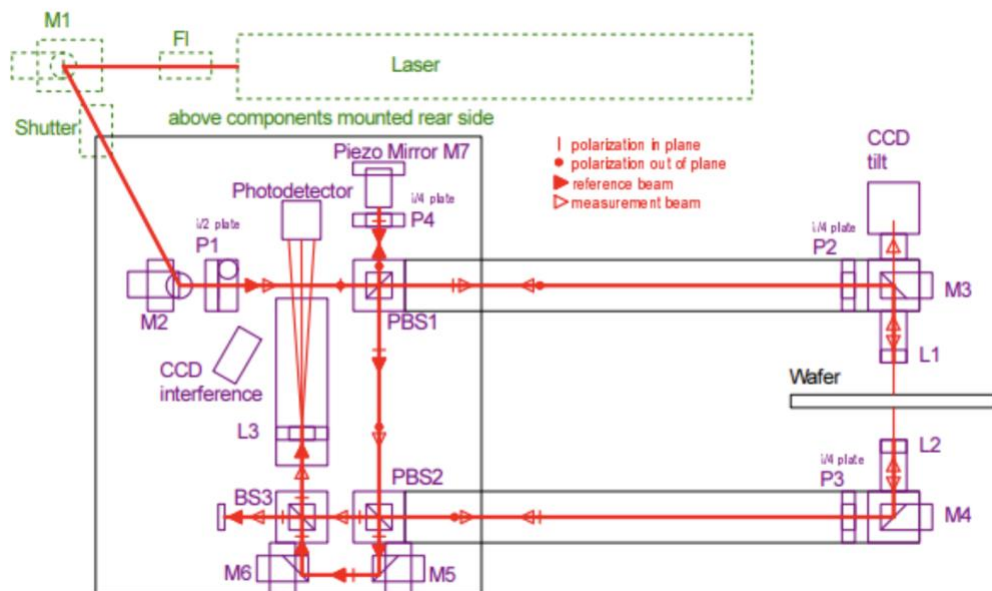


Figure 4.4 Schematic of the optical setup for the aixACCT DBLI measurement tool.

The beam is initially produced using a He-Ne laser and subsequently traverses a diaphragm and a shutter before being redirected into the primary optical pathway by mirrors M1 and M2. Subsequently, the incident light undergoes polarization by the utilization of the $\lambda/2$ plate P1, after which it proceeds towards the initial polarizing beam splitter (PBS1). This beam splitter effectively separates the incident light into two distinct beams, namely the measurement beam and the reference beam. A polarizing beam splitter (PBS) exhibits the property of reflecting incident light with Y-polarization while allowing the transmission of light with X-polarization, where X and Y represent the directions of the Cartesian axis. The measurement beam is the transmitted beam that undergoes a longer path relative to the reference beam, resulting in increased losses. The incident beam traverses the $\lambda/4$ plate P2, undergoes reflection at the mirror

M3, and is thereafter concentrated onto the upper surface of the wafer through the use of the lens L1. The incident light is reflected and returns, subsequently passing through the P2 plate once more. As a result, the polarization of the light is altered from the X-direction to the Y-direction. The reflected light passes through PBS1 and PBS2, subsequently reaching the $\lambda/4$ plate P3, mirror M4, and lens L2. Finally, the light is focused onto the bottom surface of the wafer. The system is divided into two components: the measuring beam and the reference beam. A polarizing beam splitter (PBS) exhibits the property of reflecting incident light that possesses Y-polarization while allowing the transmission of light with X-polarization. Here, X and Y represent the orientations along the Cartesian axes. The measurement beam is the transmitted beam that undergoes a longer path relative to the reference beam, resulting in greater susceptibility to losses. The incident beam traverses the $\lambda/4$ plate P2, undergoes reflection at the mirror M3, and is thereafter concentrated onto the upper surface of the wafer through the utilization of lens L1. Subsequently, the incident light is reflected and returns, traversing the P2 plate once more, resulting in a change in polarization from the X-direction to the Y-direction. The reflected light passes through PBS1 and PBS2, subsequently reaching the $\lambda/4$ plate P3, mirror M4, and lens L2. Finally, the light is focused onto the bottom surface of the wafer. This tool can perform all of the ferroelectric thin film characterization measurements like Dynamic Hysteresis Measurement (DHM), Piezo Measurement (PZM), Capacitance Voltage Measurement (CVM), Pulse Measurement (PM) etc. The PZM mode was employed in order to determine the piezo coefficient (d_{33}) of the materials under investigation.

4.2.3 d_{33} measurement

The Piezo Measurement method utilizes the DBLI system to capture the displacement of the film, which is detected through the changes in the interference fringes on the photodetector. To get the d_{33} value, it is necessary to position the laser spot precisely at the center of the pad. Additionally, the probe should be oriented on its side to minimize any scattering of the beam's light. Figure 4.5 illustrates an instance of the probing and laser positioning process performed on a circular capacitor with a diameter of 3 mm.

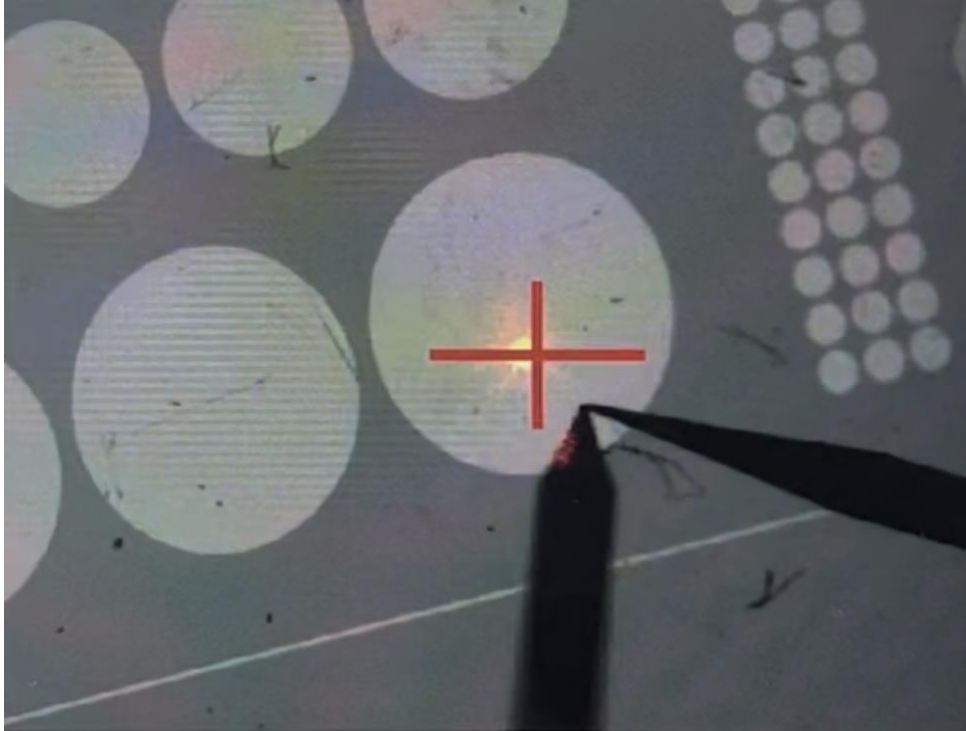


Figure 4.5 A demonstration of the laser placement and examination of a 3 mm circle ferroelectric capacitor.

Using the PZM mode of measurement, Polarization-displacement contours in the time domain have been obtained for various circles. The amplitude voltage was 20 V, and the frequency of signal was 1 kHz. On average, 500 complete cycles were measured for each circular pad, which contributed to the noise reduction. Each sample's d_{33} value is displayed in table 4.1.

Table 4.1 d_{33} value extracted from our samples using aixACCT DBLI.

Sample Label	Sc (%)	d_{33} value (pm/V)
3.01	10	6.6
3.03	20	10.1
3.05	30	13.5
3.07	40	10.4
3.09	45	6.55
3.11	35	11.6

Based on the data shown in Table 4.1, it is evident that the d_{33} value of the films exhibited a progressive increase as the Sc doping level climbed up to 30%. However, above this threshold, the d_{33} value exhibited a subsequent reduction in accordance with the increasing order of Sc doping percentage. Despite obtaining lower values of d_{33} than first expected, our results align with the observed d_{33} changing pattern reported in the study conducted by AKIYAMA et al. [36]. However, Olsson et al. (2020) demonstrated a gradual rise in the d_{33} values of *ScAlN* films as the Sc% increased, up to a threshold of 45% [37]. It was observed that there were significant variations in the pattern of the samples and the factors governing the deposition process. To investigate the underlying cause of getting smaller values of d_{33} , we assumed a couple of facts and theories including polarization reversal, wake up process, deposition control parameters, cleaning methods, bottom electrode connection method and as well as considering full 8" wafer deposition. To confirm our assumptions or to improve the piezoelectric property of *ScAlN* films, further investigation is required.

The data from table 4.1 is plotted show to the variation of d_{33} values with the change of Sc to Al power ratio which indicates the Sc doping level in our films. Figure 4.6 depicts the change of d_{33} values with the Sc to Al target generator power ratio.

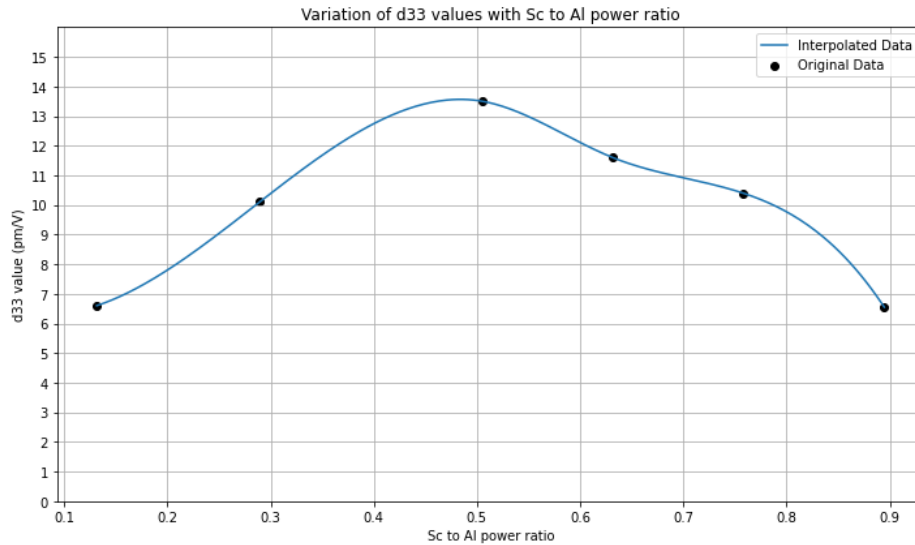


Figure 4.6 Change in d_{33} values with Sc to Al generator power ratio.

4.3 Polarization-Displacement curve

After the d_{33} measurement the polarization – displacement curve in time domain was exported for each sample. Figure 4.7 represents the polarization – displacement curve in time domain for $Sc_xAl_{1-x}N$; where $x = 0.1, 0.2, 0.3, 0.4, 0.45, 0.35$. These are the averages of 500 cycles of measurements for each sample.

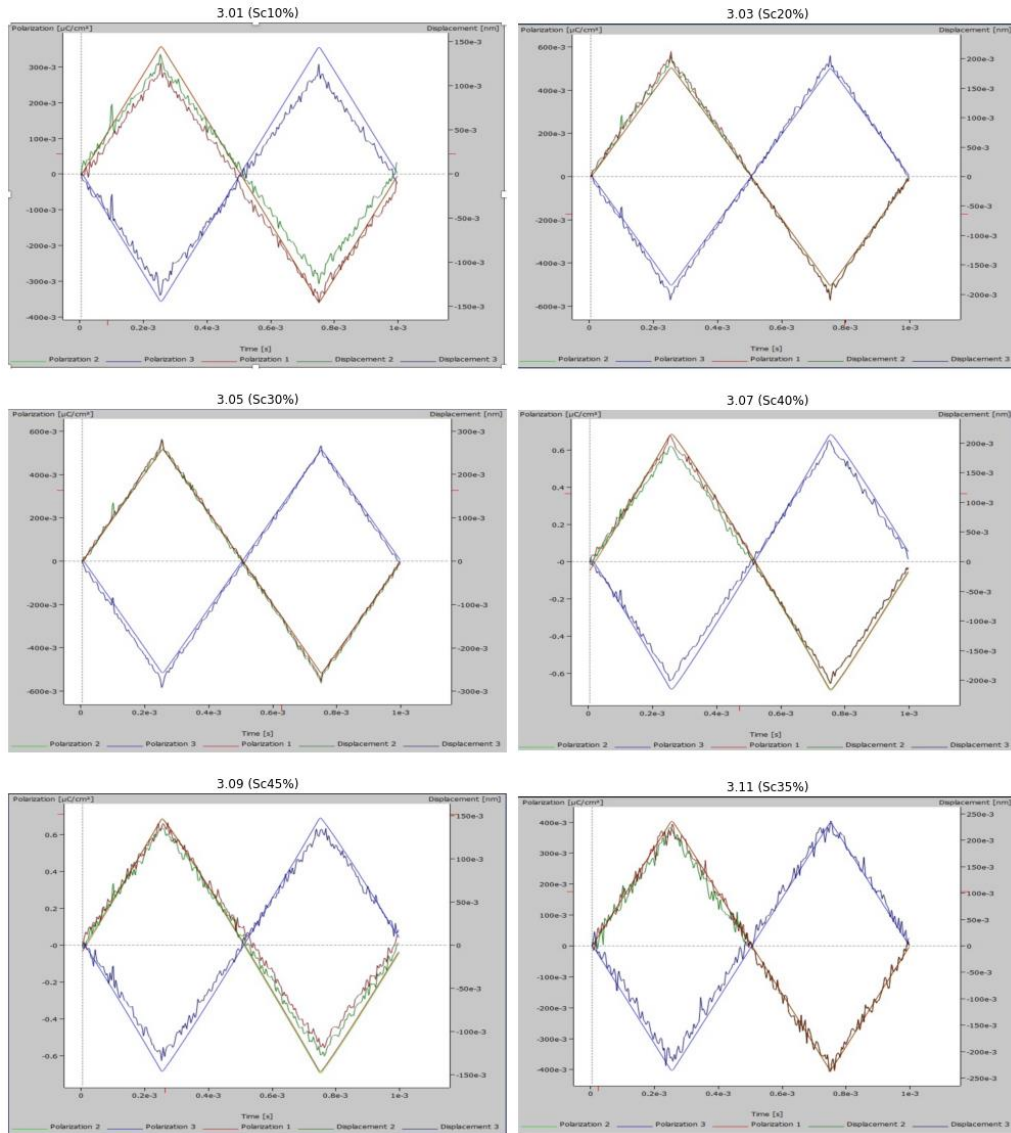


Figure 4.7 polarization – displacement curve in time domain for our $ScAlN$ samples with different Sc%

We can notice it reduced the noise level in a significant level. For 30% Sc doped $ScAlN$ chip, smallest amount of noise has been observed. Furthermore, this chip gave the highest d_{33} value among all the samples.

Chapter 5: Conclusions and future research scopes

This chapter presents a brief analysis of the significant findings and achievements resulting from the investigative research conducted. Additionally, this study will provide insight into potential areas for future research in light of the findings obtained during this investigation. Additional research is necessary in order to address the limitations inherent in our investigations and bridge the discrepancies observed between the expected outcomes and the actual values obtained during experimentation.

This research study has successfully produced experimental data pertaining to the fabrication and characterization of *ScAlN* thin films. The impact of deposition control factors on the sputtering process has been investigated, and optimal values for these variables have been identified. The optimal deposition rate for a specific concentration of Sc-doped sputtering target has been experimentally determined, serving as a reference for predicting the desired thickness in future deposition processes. We received insight on the impact of deposition factors on film stresses. If it is necessary to modify the thickness to a slightly tensile or compressive mode, these findings can assist in determining the specific parameters that should be regulated and the corresponding rates at which they should be adjusted. Manipulating the parameters can also impact the surface characteristics and crystallographic arrangement of the film. The impact of control parameters and the doping rate of Scandium on the quality of film surface and crystallographic structure was investigated and studied. The clarity of the crystallographic phase orientation and structural overview was obtained by measuring the values and fluctuation of the crystal structure with respect to the Sc% content. The impact of Sc doping on the identification of distinct phases within a specific film can be studied. Additionally, the impact of Platinum (Pt), Aluminum (Al) and Tungsten (W) as a bottom electrode layer on the determination of film quality was explored. The high precision microscopy carried out during our investigation provided us with visual representations of the surface topography, as well as information about the levels of film roughness. During our study, we acquired knowledge on the abnormal growth patterns exhibited by lattice structures in films, as well as the impact of Sc doping on these structures. Finally, we conducted measurements of the d_{33} values of our films, which serve as an indicator of their piezoelectric behavior. We also attempted to assess the ferroelectric properties of the aforementioned films; however, we encountered challenges as the samples exhibited inadequate reaction, rendering us unable to get conclusive measurements. This observation facilitated our comprehension of several aspects, including the wake-up process of a specific polarization mode and the maximum voltage response of the films. This prompted us to form conjectures regarding the impact of depositing the film on whole wafers, fragmented chips, or employing carrier wafers. The assumptions in our study encompass the analysis of various crystallographic phase orientations, which are now being explored as part of our research agenda. The applying voltage limitations prompted us to proceed with the measurement of ferroelectric properties in our films. Based on the obtained measurement results and the limits encountered during our analysis, these assumptions prompted us to undertake additional research

on the topics mentioned above. The potential for future research in these areas is significant due to the limited number of past investigations conducted prior to our study. Moreover, the ferroelectric characteristics of *ScAlN* have been recently discovered. The incorporation of additional substances, such as Boron (B), into a material might result in significant enhancements in its properties, thereby aligning with our desired objectives. This region is relatively new and holds significant potential for future research endeavors aimed at enhancing the materials used in Bulk Acoustic Resonators (BAWR) and other associated applications.

Bibliography

- [1] MEMS Explained – A Comprehensive Guide to Microelectromechanical Systems. Nanowork website. <https://www.nanowork.com/mems-explained.php/> (Accessed on 2023-07-03)
- [2] Status of the MEMS Industry 2018 - Yole Développement, Yole Group, 2018, [https://medias.yolegroup.com/uploads/2019/01/YD18019_Status_of_the MEMS Industry 2018_sample-1.pdf](https://medias.yolegroup.com/uploads/2019/01/YD18019_Status_of_the_MEMS_Industry_2018_sample-1.pdf) (Accessed on 2023-07-03)
- [3] Campanella, H. Acoustic Wave and Electromechanical Resonators: Concept to Key Applications; Artech House: Norwood, MA, USA, 2010, pp 1-33.
- [4] W. T. Hsu; K. Hashmi; Resonators, Oscillators, and Frequency References. Reference Module in Materials Science and Materials Engineering. Elsevier. 2016, 9780128035818. DOI: [10.1016/B978-0-12-803581-8.10112-2](https://doi.org/10.1016/B978-0-12-803581-8.10112-2).
- [5] Liu, Y.; Cai, Y.; Zhang, Y.; Tovstopyat, A.; Liu, S.; Sun, C. Materials, Design, and Characteristics of Bulk Acoustic Wave Resonator: A Review. *Micromachines*. 2020, *11*, 630. DOI: [10.3390/mi11070630](https://doi.org/10.3390/mi11070630)
- [6] Ajay, K; Rahul, P. The potential of acoustic wave devices for gas sensing applications. *Sensors and Actuators A: Physical*. Volume 339. 2022, 113498, 0924-4247, DOI: [10.1016/j.sna.2022.113498](https://doi.org/10.1016/j.sna.2022.113498)
- [7] Piazza, G. Piezoelectric Resonant MEMS. Resonant MEMS: Fundamentals, Implementation and Application. [Advanced Micro and Nanosystems](https://doi.org/10.1002/9783527676330.ch7). Wiley-VCH Verlag GmbH & Co. KGaA, 2015, pp 147-171. DOI: [10.1002/9783527676330.ch7](https://doi.org/10.1002/9783527676330.ch7)
- [8] Zhang, Z.; Liang, J.; Zhang, D.; Pang, W.; Zhang, H. A Novel Bulk Acoustic Wave Resonator for Filters and Sensors Applications. *Micromachines* 2015, *6*, 1306-1316. DOI: [10.3390/mi6091306](https://doi.org/10.3390/mi6091306)
- [9] D. Damjanovic, Piezoelectricity, Editor(s): Franco Bassani, Gerald L. Liedl, Peter Wyder, Encyclopedia of Condensed Matter Physics, Elsevier, 2005, Pages 300-309, ISBN 9780123694010, DOI: [10.1016/B0-12-369401-9/00433-2](https://doi.org/10.1016/B0-12-369401-9/00433-2).
- [10] Cui, C., Xue, F., Hu, WJ. et al. Two-dimensional materials with piezoelectric and ferroelectric functionalities. *npj 2D Mater Appl* 2, 18 (2018). DOI:[10.1038/s41699-018-0063-5](https://doi.org/10.1038/s41699-018-0063-5)
- [11] Rupitsch, S.J. (2019). Piezoelectricity. In: Piezoelectric Sensors and Actuators. Topics in Mining, Metallurgy and Materials Engineering. Springer, Berlin, Heidelberg. DOI: [10.1007/978-3-662-57534-5_3](https://doi.org/10.1007/978-3-662-57534-5_3)
- [12] Simon Fichtner; Niklas Wolff; Fabian Lofink; Lorenz Kienle; Bernhard Wagner. AlScN: A III-V semiconductor-based ferroelectric. *Journal of Applied Physics* 125, 114103 (2019). DOI: [10.1063/1.5084945](https://doi.org/10.1063/1.5084945)
- [13] Giribaldi, Gabriel. Sc-doped AlN: high performance piezoelectric MEMS resonators and high-polarization ferroelectric. PhD diss., Politecnico di Torino, 2020. <https://webthesis.biblio.polito.it/secure/16167/1/tesi.pdf>. (Accessed 2023-09-29)
- [14] Damjanovic, Dragan. (1998). Ferroelectric, Dielectric and Piezoelectric Properties of Ferroelectric Thin Films and Ceramics. *Reports on Progress in Physics*, Volume 61, Number 9. DOI: [10.1088/0034-4885/61/9/002](https://doi.org/10.1088/0034-4885/61/9/002).
- [15] Eric Cross, L. (1993). Ferroelectric Ceramics: Tailoring Properties for Specific Applications. In: Setter, N., Colla, E.L. (eds) *Ferroelectric Ceramics*. Monte Verità. Birkhäuser Basel. DOI: [10.1007/978-3-0348-7551-6_1](https://doi.org/10.1007/978-3-0348-7551-6_1)
- [16] Sawyer, C. B. and Tower, C. H. Rochelle Salt as a Dielectric. *Physical Review*, volume 35, issue 3, pp 269 - 273. American Physical Society. Feb 1930. DOI: [10.1103/PhysRev.35.269](https://doi.org/10.1103/PhysRev.35.269)
- [17] Burfoot, J.C. and Taylor (1979) *Polar Dielectrics and Their Applications*. Macmillan Press, London.

- [18] Zhou Q, Lau S, Wu D, Shung KK. Piezoelectric films for high frequency ultrasonic transducers in biomedical applications. *Prog Mater Sci.* 2011 Feb;56(2):139-174. DOI: [10.1016/j.pmatsci.2010.09.001](https://doi.org/10.1016/j.pmatsci.2010.09.001).
- [19] Kenji Uchino. *Advances in ceramic actuator materials*. Materials Letters, Volume 22, Issues 1–2, 1995, Pages 1-4, ISSN 0167-577X. DOI: [10.1016/0167-577X\(94\)00231-2](https://doi.org/10.1016/0167-577X(94)00231-2)
- [20] Adel Bendjerad & Boukhtache, S. & Benhaya, A. & Luneau, Dominique & El, Hak & Benyahia, Kaddour. (2016). Modeling of magnetic properties of iron thin films deposited by RF magnetron sputtering using Preisach model. *Serbian Journal of Electrical Engineering.* 13. 229-238. DOI: [10.2298/SJEE1602229B](https://doi.org/10.2298/SJEE1602229B).
- [21] Evatec Process System website. Product details of CLUSTERLINE 200. <https://evatecnet.com/products/clusterline-family/clusterline-200/>. (Accessed on 2023-08-07)
- [22] R. Beaucejour; V. Roebisch; A. Kochhar; C. G. Moe; M. D. Hodge and R. H. Olsson. Controlling Residual Stress and Suppression of Anomalous Grains in Aluminum Scandium Nitride Films Grown Directly on Silicon. *Journal of Microelectromechanical Systems*, vol. 31, no. 4, pp. 604-611, Aug. 2022. DOI: [10.1109/JMEMS.2022.3167430](https://doi.org/10.1109/JMEMS.2022.3167430).
- [23] Ellipsometer Description. Research facilities and equipment description. Texas state university, College of Science and Engineering website. <https://sro.txst.edu/fac/arsc/equipment/spectroscopy/ellipsometer.html>. (Accessed on 2023-08-08)
- [24] Film-Stress-Tencor-FLX-2320-Spec-Sheet. Website of Nanofabrication group, University of Utah. <https://www.nanofab.utah.edu/wp-content/uploads/2022/12/Film-stress-Tencor-FLX2320-Spec-Sheet.pdf>. (Accessed on 2023-08-09)
- [25] Tencor FLX-2320 Thin Film Stress Measurement webpage. Website of Wisconsin Centers for Nanoscale Technology, The University of Wisconsin–Madison. <https://wcnt.wisc.edu/nanofabrication/metrology/flx-2320-thin-film-stress-measurement/> (Accessed on 2023-08-09)
- [26] G, Adaikala Selvan; S, Rachel; T, Gajendran. *Several assorted characterization methods of nanoparticles*. Nanomaterials. Academic Press, 2021, Pages 301-308. ISBN 9780128224014. DOI: [10.1016/B978-0-12-822401-4.00040-4](https://doi.org/10.1016/B978-0-12-822401-4.00040-4).
- [27] Specification of the x-pert pro mpd webpage from Studylib.net website. <https://studylib.net/doc/6729333/specification-of-the-x-pert-pro-mpd>. (Accessed on 2023-08-10)
- [28] Huy, Hoang & Tran, Van & Thien Huynh, Tai & Ho, Van. (2016). Preparation and characterization of high-dispersed pt/c nano-electrocatalysts for fuel cell applications. *Journal of Science and Technology.* 54. DOI: [10.15625/0866-708X/54/4/7308](https://doi.org/10.15625/0866-708X/54/4/7308).
- [29] Zhao, Qing-Xiang & Xu, Xiaolong & Wang, Zhijun & Yu, Dapeng. (2004). Field emission from AlN nanoneedle arrays. *Applied Physics Letters.* 85. 5331-5333. DOI: [10.1063/1.1825620](https://doi.org/10.1063/1.1825620).
- [30] Purdu University Research Equipment webpage. <https://www.purdue.edu/ehps/rem/laboratory/equipment%20safety/Research%20Equipment/sem.html#:~:text=The%20SEM%20is%20a%20microscope,much%20bigger%20variety%20of%20specimens>. (Accessed on 2023-08-10)
- [31] Suprakas Sinha Ray. *Structure and Morphology Characterization Techniques*. Editor(s): Suprakas Sinha Ray, *Clay-Containing Polymer Nanocomposites*, Elsevier, 2013. Chapter 3, Pages 39-66. ISBN 9780444594372. DOI: [10.1016/B978-0-444-59437-2.00003-X](https://doi.org/10.1016/B978-0-444-59437-2.00003-X).
- [32] Ravi Rao. *Atomic Force Microscopy Explained: Principles, Construction, Working, and Applications*. WEVOLVER Website. 08 October 2021. <https://www.wevolver.com/article/atomic-force-microscopy-explained-principles-construction-working-and-applications> (Accessed on 2023-08-13)

- [33] Park XE-7 AFM specifications. Park Systems Website. <https://www.parksystems.com/75-products/park-xe7>. (Accessed on 2023-08-14)
- [34] K. Umeda; H. Kawai; A. Honda; M. Akiyama; T. Kato; T. Fukura. Piezoelectric properties of ScAlN thin films for piezo-MEMS devices. 2013. IEEE 26th International Conference on Micro Electromechanical Systems (MEMS), Taipei, Taiwan, 2013, pp. 733-736. DOI: [10.1109/MEMSYS.2013.6474347](https://doi.org/10.1109/MEMSYS.2013.6474347).
- [35] Akiyama, M.; Kamohara, T.; Kano, K.; Teshigahara, A.; Takeuchi, Y.; Kawahara, N. (2009). Enhancement of Piezoelectric Response in Scandium Aluminum Nitride Alloy Thin Films Prepared by Dual Reactive Cosputtering. *Advanced Materials.*, 21(5), 593–596. DOI: [10.1002/adma.200802611](https://doi.org/10.1002/adma.200802611)
- [36] Morito AKIYAMA et al. Preparation of scandium aluminum nitride thin films by using scandium aluminum alloy sputtering target and design of experiments. *Journal of the Ceramic Society of Japan*. 2010. Volume 118, number 1384, pp. 1166-1169. DOI: [10.2109/jcersj2.118.1166](https://doi.org/10.2109/jcersj2.118.1166)
- [37] R. H. Olsson; Z. Tang; M. D'Agati. Doping of Aluminum Nitride and the Impact on Thin Film Piezoelectric and Ferroelectric Device Performance. IEEE Custom Integrated Circuits Conference (CICC), Boston, MA, USA, 2020, pp. 1-6. DOI: [10.1109/CICC48029.2020.9075911](https://doi.org/10.1109/CICC48029.2020.9075911).
-

Statement of non-plagiarism

I hereby declare that all information in this report has been obtained and presented in accordance with academic rules and ethical conduct and the work I am submitting in this report, except where I have indicated, is my own work.

Kapil Saha

Date: August 18, 2023



Supervisor approval

I, the undersigned, Dr. Pietro Simeoni, supervisor of Kapil Saha, student of the PSRS EMJMD, during his master thesis at SMART Center, Northeastern University, certify that I approve the content of this master thesis report entitled “Characterization of Scandium doped Aluminum Nitride thin films for Bulk Acoustic Wave Resonators”.

A handwritten signature in black ink, appearing to read 'P. Simeoni', with a horizontal line extending to the right.

22 August 2023

Date and signature

Copyrights

[1] Figure 1.1 is reused under a license agreement between Kapil Saha and Springer Nature using Copyright Clearance Center.

License number: 5591430174154.

License date: Jul 17, 2023

Type of Use: Republish in a Thesis/Dissertation

Licensed Content Publisher: Springer Nature

Licensed Content Author: Stefan Johann Rupitsch

Licensed Content Title: Piezoelectricity

Licensed Content Date: Jan 1, 2019.

[2] Figure 1.2 and Figure 1.3 are reused under a license agreement between Kapil Saha and Copyright Clearance Center, Inc. ("CCC") on behalf of Rightsholder.

License number: 1385361-1.

ISSN: 0034-4885

License date: 11-Aug-2023

Type of Use: Republish in a Thesis/Dissertation

Licensed Content Publisher: IOP Publishing, Ltd

Licensed Content Publication Title: Reports on Progress in Physics

Content Author: Dragan Damjanovic

Content Title: Ferroelectric Properties

Content Publication Date: May 5, 1998.

[3] Figure 4.1 is reused under a license agreement between Kapil Saha and AIP Publishing using Copyright Clearance Center.

License number: 5612761235356.

License date: Aug 19, 2023

Type of Use: Republish in a Thesis/Dissertation

Licensed Content Publisher: AIP Publishing

Licensed Content Publication: Journal of Applied Physics

Licensed Content Author: Fichtner, Simon; Wolff, Niklas

Licensed Content Title: AlScN: A III-V semiconductor-based ferroelectric.

Licensed Content Date: Mar 18, 2019.